



## Magnetically separable $\text{Mn}_x\text{Zn}_{1-x}\text{Fe}_2\text{O}_4$ ; ( $0.0 \leq x \leq 0.5$ ) nanostructures: Structural, morphological, opto-magnetic and photocatalytic properties

A. Manikandan & S. Arul Antony

To cite this article: A. Manikandan & S. Arul Antony (2015): Magnetically separable  $\text{Mn}_x\text{Zn}_{1-x}\text{Fe}_2\text{O}_4$ ; ( $0.0 \leq x \leq 0.5$ ) nanostructures: Structural, morphological, opto-magnetic and photocatalytic properties, *Synthesis and Reactivity in Inorganic, Metal-Organic, and Nano-Metal Chemistry*, DOI: [10.1080/15533174.2015.1004454](https://doi.org/10.1080/15533174.2015.1004454)

To link to this article: <http://dx.doi.org/10.1080/15533174.2015.1004454>



Accepted author version posted online: 22 Dec 2015.



Submit your article to this journal [↗](#)



Article views: 2



View related articles [↗](#)



View Crossmark data [↗](#)

**Magnetically separable  $Mn_xZn_{1-x}Fe_2O_4$ ; ( $0.0 \leq x \leq 0.5$ ) nanostructures: Structural, morphological, opto-magnetic and photocatalytic properties**

A. Manikandan<sup>1,\*</sup>, S. Arul Antony<sup>1,#</sup>

<sup>1</sup>PG and Research Department of Chemistry, Presidency College, Chennai 600 005, India

\*Corresponding author Email: mkavath15@gmail.com

#Corresponding author E-mail: antonypresidency15@gmail.com

**Abstract**

$Mn^{2+}$  doped  $ZnFe_2O_4$  nano-crystals (NCs) have been successfully synthesized by one-pot auto combustion method. The as-synthesized  $Mn_xZn_{1-x}Fe_2O_4$  NCs were characterized by XRD, FT-IR, HR-SEM, TEM, EDX, BET, DRS, PL and VSM. The results indicated that the as-prepared spinel  $Mn_xZn_{1-x}Fe_2O_4$  NCs showed high crystallinity and uniform size distribution with particle-like morphologies. The present study leads to enhance the photocatalytic activity of  $Mn_xZn_{1-x}Fe_2O_4$  with the addition of  $TiO_2$ . Having established that spinel  $Mn_xZn_{1-x}Fe_2O_4$  was photo-catalytically active, the mixed oxide catalysts of  $Mn_xZn_{1-x}Fe_2O_4 -TiO_2$  were also tested for the photocatalytic degradation (PCD) of 4-Chlorophenol (4-CP).

**Keywords**

Ferrites; Nano-crystals; X-ray diffraction; Opto-Magnetic properties; Photo-catalyst

## 1. Introduction

Recently, spinel-type nanostructured semiconducting magnetic materials with the general formula  $M^{2+}(Fe^{3+})_2O_4$ : where  $M^{2+} = Mn^{2+}, Co^{2+}, Ni^{2+}, Cu^{2+}, Zn^{2+}$ , etc. have become an important area in nano-science and nanotechnology, due to their unique physical and chemical properties than that of their bulk counterparts [1]. These properties are exploited in technological applications like magnetic devices, switching devices, microwave absorbers, active components of ferrofluids, permanent magnets, color imaging, magnetic refrigeration, biomedicine, drug delivery, magnetic resonance imaging (MRI), anti-cancer drugs, magnetic cell separation, recording media and photo-catalyst [2-10].

$ZnFe_2O_4$  is a normal spinel structure and has been reported as a semiconducting material, where  $Zn^{2+}$  preferably occupies the tetrahedral (A-) sites, due to their affinity for  $sp^3$  bonding with  $O^{2-}$  anions leaving all the  $Fe^{3+}$  ions on the octahedral (B-) sites. Also,  $ZnFe_2O_4$  is paramagnetic in nature at room temperature [11], due to weak super exchange interaction attributed to  $90^\circ$  angle in  $Fe^{3+}-O-Fe^{3+}$  [12].  $ZnFe_2O_4$  is soft ferrite and are very useful in microwave applications, high quality filter, radio frequency circuits, transformer cores, read/write heads for high speed digital tapes and photo-catalyst [9]. Various techniques have been used for the preparation of nano-crystalline spinel ferrites, such as co-precipitation, sol-gel, mechanical alloying, hydrothermal, ball milling and ultra sonic cavitation [9, 13-15] methods. Rath et al. [16] have reported the dependence on cation distribution of particle size, lattice parameter and magnetic properties in nanosized Mn-Zn ferrite with different concentration of Zn content by a hydrothermal precipitation method. Auzans et al. [17] have reported the properties of Mn-Zn ferrite nanoparticles used for ionic and surfacted ferrofluids with different ratios of Zn

content by co-precipitation method. Azam [18] has reported the effect of Co doping on structural and electrical properties of  $\text{Co}_x\text{Cu}_{1-x}\text{Fe}_2\text{O}_4$  ( $0.0 \leq x \leq 0.5$ ) nano-particles by sol-gel method. Azam et al. [19] have reported the structural, optical and transport properties of  $\text{Al}^{3+}$  doped  $\text{BiFeO}_3$  were synthesized by solution combustion method using citric acid as fuel at a temperature as low as 200 °C. Gozuak et al. [20] and Koseoglu [21] have reported the structural, electrical and magnetic properties of  $\text{Co}_x\text{Zn}_{1-x}\text{Fe}_2\text{O}_4$  and  $\text{Mn}_x\text{Ni}_{1-x}\text{Fe}_2\text{O}_4$  nanoparticles respectively, were prepared by a PEG-assisted hydrothermal method.

However, the above conventional methods meet some disadvantages such as, the requirement of complicated equipment, high-energy consuming, and higher processing temperature and also require rather long reaction time caused by the multiple steps (calcinations) to complete the crystallization of ferrite nanostructures. For this reason, the introduction of a simple one-pot urea-assisted auto combustion method is advantageous for the synthesis of various ceramic powders, because the formation of nano-crystals, rapid processing time and low energy cost [22-24]. The spinel ferrite structure allows, introduction of different metal ions, which can change the optical, magnetic and electric properties considerably and these properties of the ferrites depend on the distribution of the cations in A- and B- sites and on the range of the deficiency in the chemical composition [25]. The magnetic properties of ferrites strongly depend on the kind and content of substituting metal ions.

$\text{ZnFe}_2\text{O}_4$  has potential applications in the conversion of sunlight and sensitive towards visible light [12]. The conduction mechanism in  $\text{ZnFe}_2\text{O}_4$  is due to the  $\text{Fe}^{2+}$  and  $\text{Fe}^{3+}$  ions present in B- sites as suggested by Feteira et al. [26]. Mostly, nano-sized  $\text{ZnFe}_2\text{O}_4$  has been extensively studied by universal researchers, because of its fashionable size dependent physical and chemical

properties as compared to bulk materials [1]. Among the other semiconductors,  $\text{ZnFe}_2\text{O}_4$  appears to be a highly promising photo-catalyst [9]. Many perovskite or spinel type complex oxides have been found to have visible-light-driven photoactivity. Among them, spinel  $\text{ZnFe}_2\text{O}_4$  with a relatively narrow band gap energy of 1.9 eV, concerned significant interest in the conversion of solar energy, photochemical hydrogen production from water and photo-catalysts, due to its visible-light response, good photochemical stability and low cost [27, 28]. The PCD of 4-chloro phenol (4-CP) has been investigated for different concentration of  $\text{Mn}^{2+}$  doped  $\text{ZnFe}_2\text{O}_4$  catalyst with  $\text{TiO}_2$  and the observed photocatalytic activity is correlated with the physicochemical properties. It has been reported that a coupled semiconductor of  $\text{TiO}_2$ - $\text{ZnFe}_2\text{O}_4$  exhibits visible light photocatalytic activity as  $\text{ZnFe}_2\text{O}_4$  can absorb visible light and transfer the photogenerated electron to  $\text{TiO}_2$ , due to the comparable conduction band potentials of these two catalysts [29]. However, it is known that  $\text{ZnFe}_2\text{O}_4$  alone is photocatalytically inactive under visible-light irradiation. A core-shell type cobalt ferrite coated with silica and titania exhibited photo-degradation activity for methyl orange comparable to that of heated sample and P-25  $\text{TiO}_2$  [30]. Though, this coupled photocatalyst showed visible light activity for the photo-degradation of organic pollutants, it is seen that its visible light activity is privileged. Chung et al. [31] have synthesized  $\text{TiO}_2$ - $\text{NiFe}_2\text{O}_4$  and  $\text{TiO}_2$ - $\text{SiO}_2$ - $\text{NiFe}_2\text{O}_4$  magnetic nano-composites by a multistep spray pyrolysis process and found that the titania-silica layered particles showed better photocatalytic activity for methylene blue degradation compared to titania alone on nickel ferrite. Lee et al. [32] synthesized barium ferrite-silica-titania composite photocatalyst by precipitation method showed photocatalytic activity for the degradation of Procion red MX-5B dye under UV illumination and the photocatalytic activity increased after heat treatment at 773 K due to the

improved crystallinity of the heat treated sample. Xu et al. [27] have reported the photocatalytic properties of visible-light-active  $\text{ZnFe}_2\text{O}_4$ -doped  $\text{TiO}_2$  photocatalyst. Hankare et al. [10] have reported  $\text{TiO}_2\text{-Al}_2\text{O}_3\text{-ZnFe}_2\text{O}_4$  for photocatalytic activity for the degradation of methyl red and thymol blue as compared to  $\text{TiO}_2\text{-ZnFe}_2\text{O}_4$  composite and  $\text{ZnFe}_2\text{O}_4$ . Fu et al. [33] have reported magnetically separable  $\text{ZnFe}_2\text{O}_4$ -graphene nanocomposite photocatalyst with different graphene content was prepared by a facile one-step hydrothermal method and the photodegradation rate of methylene blue was 88% after visible light irradiation for only 5 min and reached up to 99% after irradiation for 90 min. Xiong et al. [34] report a facile strategy to fabricate a  $\text{CdS-MFe}_2\text{O}_4$  nanocomposite with differing ferrite content via a two-step hydrothermal method and the photocatalytic activities of as-prepared photocatalysts were evaluated by the degradation of rhodamine B and 4-CP in aqueous solution under visible-light irradiation.

When metal was doped into the spinel  $\text{ZnFe}_2\text{O}_4$ , more surface defects are produced, which hindered the recombination of photo-induced electron-hole pairs. This contributed to the improvement of the photocatalytic activity. Even though,  $\text{TiO}_2$  is most extensively investigated photo-catalyst, civilizing its quantum efficiency is still a major challenge. The enhancement of photocatalytic activity of  $\text{TiO}_2$  can be achieved by doping with metals, the addition of electron donors to the reaction system, and the addition of other semiconductor oxides in order to reduce the charge carrier recombination [35]. It has been reported that the addition of  $\text{Mn}_x\text{Zn}_{1-x}\text{Fe}_2\text{O}_4$  to  $\text{TiO}_2$  can increase the surface area and hydroxyl groups in  $\text{Mn}_x\text{Zn}_{1-x}\text{Fe}_2\text{O}_4\text{-TiO}_2$  mixed catalysts which, in turn, improves the quantum efficiency of  $\text{TiO}_2$  [36]. Moreover,  $\text{Mn}_x\text{Zn}_{1-x}\text{Fe}_2\text{O}_4$  and  $\text{Mn}_x\text{Zn}_{1-x}\text{Fe}_2\text{O}_4\text{-TiO}_2$  binary oxide catalysts have been well investigated for their photocatalytic properties. Such advanced  $\text{Mn}_x\text{Zn}_{1-x}\text{Fe}_2\text{O}_4\text{-TiO}_2$  mixed oxides extend their application through

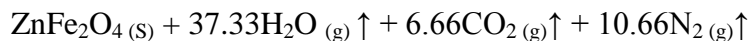
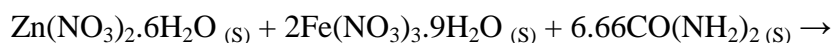
the generation of new catalytic sites, due to a strong interaction between them. Therefore, it is highly interesting and desirable to study the photocatalytic activity of  $\text{Mn}_x\text{Zn}_{1-x}\text{Fe}_2\text{O}_4\text{-TiO}_2$  mixed oxides.

## 2. Experimental

### 2.1. Materials and methods

All the chemicals used in this study were of analytical grade obtained from Merck, India and were used as received without further purification. Zinc nitrate ( $\text{Zn}(\text{NO}_3)_2 \cdot 6\text{H}_2\text{O}$ , 98%), manganese nitrate ( $\text{Mn}(\text{NO}_3)_2 \cdot 4\text{H}_2\text{O}$ , 98%), ferric nitrate ( $\text{Fe}(\text{NO}_3)_3 \cdot 9\text{H}_2\text{O}$ , 98%) and urea ( $\text{CO}(\text{NH}_2)_2$ ) as the fuel are used for this auto combustion method. The samples were prepared with the addition of  $\text{Mn}^{2+}$  of different molar ratios ( $\text{Mn}_x\text{Zn}_{1-x}\text{Fe}_2\text{O}_4$ ;  $x = 0.0, 0.1, 0.2, 0.3, 0.4$  and  $0.5$ ) to  $\text{ZnFe}_2\text{O}_4$ . Metal nitrates and urea were dissolved separately in 20 ml of de-ionized water and poured into a beaker and stirred using magnetic stirrer for 15 minutes to obtain clear solution. In case of  $\text{ZnFe}_2\text{O}_4$ , the precursor solution was taken in the silica crucible and treated in an air furnace at  $400^\circ\text{C}$  for 2h at a heating rate of  $5^\circ\text{C}/\text{min}$ , and cooled at the same rate, it became solid. The preparation procedure of urea assisted auto combustion method was given in Scheme 1. Initially, the mixture was subjected to boiling and underwent evaporation followed by the decomposition with the evolution of gases. When the solution reached the point of spontaneous combustion, it vaporized and instantly became a solid. After the completion of the combustion reaction, the solid powder was obtained and then it was washed with ethanol and dried at  $70^\circ\text{C}$  for 1 h. The as-prepared nanocrystals,  $\text{Mn}_x\text{Zn}_{1-x}\text{Fe}_2\text{O}_4$  with  $x = 0.0, 0.1, 0.2, 0.3, 0.4$  and  $0.5$ , were labeled as  $\text{ZnFe}_2\text{O}_4$ ,  $\text{Mn}_{0.1}\text{Zn}_{0.9}\text{Fe}_2\text{O}_4$ ,  $\text{Mn}_{0.2}\text{Zn}_{0.8}\text{Fe}_2\text{O}_4$ ,  $\text{Mn}_{0.3}\text{Zn}_{0.7}\text{Fe}_2\text{O}_4$ ,  $\text{Mn}_{0.4}\text{Zn}_{0.6}\text{Fe}_2\text{O}_4$  and  $\text{Mn}_{0.5}\text{Zn}_{0.5}\text{Fe}_2\text{O}_4$ , respectively.

The expected urea assisted auto combustion reaction may be as follows,



## 2.2. Characterization techniques

The structural characterization of Mn-doped  $\text{ZnFe}_2\text{O}_4$  ( $\text{Mn}_x\text{Zn}_{1-x}\text{Fe}_2\text{O}_4$  with  $x = 0.0, 0.1, 0.2, 0.3, 0.4$  and  $0.5$ ) nanocrystals were performed using Rigaku Ultima X-ray diffractometer equipped with Cu-K $\alpha$  radiation ( $\lambda = 1.5418 \text{ \AA}$ ). Structural refinements using the Rietveld method was carried out by PDXL program; both refined lattice parameters and crystallite size of the obtained ferrites were reported. The surface functional groups were analyzed by Perkin Elmer FT-IR spectrometer. Morphological studies and energy dispersive X-ray analysis of pure and Mn-doped  $\text{ZnFe}_2\text{O}_4$  nanocrystals have been performed with a Jeol JSM6360 high resolution scanning electron microscopy. The transmission electron micrographs were carried out by Philips-TEM (CM20). The surface area was derived from the  $\text{N}_2$  adsorption-desorption isotherms using liquid nitrogen at 77 K using an automatic adsorption instrument (Quantachrome Corp. Nova-1000 gas sorption analyzer). The UV-Visible diffuse reflectance spectrum was recorded using Cary100 UV-Visible spectrophotometer to estimate their band gap energy ( $E_g$ ). The photoluminescence properties were recorded at room temperature using Varian Cary Eclipse Fluorescence Spectrophotometer. Magnetic measurements were carried out at room temperature using a PMC MicroMag 3900 model vibrating sample magnetometer equipped with 1 Tesla magnet.

## 2.3. Photocatalytic reactor setup and degradation procedure

Photocatalytic degradation (PCD) experiments were carried out in a self-designed photocatalytic reactor and the schematic diagram of the photocatalytic reactor is shown in Scheme 2. The cylindrical photocatalytic reactor tube was made up of quartz/borosilicate with a dimension of 36 cm height and 1.6 cm diameter. The top portion of the reactor tube has ports for sampling, gas purging and gas outlet. The aqueous 4-Chloro phenol (4-CP) solution containing appropriate quantity of  $\text{ZnFe}_2\text{O}_4$  nano photo-catalysts was taken in the quartz/borosilicate tube and subjected to aeration for thorough mixing and placed inside the reactor setup. The lamp housing has low pressure mercury lamps (8×8 W) emitting either 254 or 365 nm with polished anodized aluminum reflectors and black cover to prevent UV leakage. Prior to photocatalytic experiments, the adsorption of 4-CP on pure  $\text{ZnFe}_2\text{O}_4$  and Mn-doped  $\text{ZnFe}_2\text{O}_4$  nano photo-catalyst was carried out by mixing 100 ml of aqueous solution of 4-CP with fixed weight of the respective photo-catalyst. This slurry was equilibrated for 30 min in a magnetic stirrer. The PCD was carried out by mixing 100 ml of aqueous 4-CP solution and fixed weight of  $\text{ZnFe}_2\text{O}_4$  nano photo-catalyst. PCD of 4-CP was also carried out with  $\text{Mn}_x\text{Zn}_{1-x}\text{Fe}_2\text{O}_4\text{-TiO}_2$  mixed oxides. A known amount of commercial  $\text{TiO}_2$  (Degussa P-25) was added to a known amount of  $\text{Mn}_x\text{Zn}_{1-x}\text{Fe}_2\text{O}_4$  and finely ground in a mortar and pestle for 30 min so as to obtain a mixture of  $\text{Mn}_x\text{Zn}_{1-x}\text{Fe}_2\text{O}_4\text{-TiO}_2$  in the required mol%. The finely ground mixture was then used directly for the PCD experiments. No heat treatment of the mixture was carried out. Therefore, the mixed oxides were actually physical mixtures and not solid solutions. Therefore, the interactions of  $\text{Mn}_x\text{Zn}_{1-x}\text{Fe}_2\text{O}_4$  with  $\text{TiO}_2$  can be assumed to be those taking place at the grain boundaries. The PCD efficiency was also calculated for pure oxides ( $\text{ZnFe}_2\text{O}_4$  and  $\text{TiO}_2$ ) and also for mixed oxides ( $\text{ZnFe}_2\text{O}_4\text{-TiO}_2$ ,  $\text{Mn}_{0.1}\text{Zn}_{0.9}\text{Fe}_2\text{O}_4\text{-TiO}_2$ ,  $\text{Mn}_{0.2}\text{Zn}_{0.8}\text{Fe}_2\text{O}_4\text{-TiO}_2$ ,  $\text{Mn}_{0.3}\text{Zn}_{0.7}\text{Fe}_2\text{O}_4\text{-TiO}_2$ ,

Mn<sub>0.4</sub>Zn<sub>0.6</sub>Fe<sub>2</sub>O<sub>4</sub>-TiO<sub>2</sub> and Mn<sub>0.5</sub>Zn<sub>0.5</sub>Fe<sub>2</sub>O<sub>4</sub>-TiO<sub>2</sub>). The experiments were performed at room temperature and the pH of the reaction mixture was adjusted (2 to 11.0 using 1 M of H<sub>2</sub>SO<sub>4</sub> and NaOH solution). Prior to irradiation, the slurry was aerated for 30 min to reach adsorption equilibrium followed by UV irradiation. Aliquots were withdrawn from the suspension at specific time intervals and centrifuged immediately at 1500 rpm. Then it was filtered through a 0.2 μm millipore filter paper to remove suspended particles. The extent of 4-CP degradation was monitored using UV-Vis spectrophotometer (Perkin-Elmer, Lamda 25). The effect of the pH of the solution was studied by adjusting the pH of the phenol solution containing the catalyst, using dilute HCl and NaOH (both from Merck, India). The pH of the solution was measured using a HANNA Phep (ModelH198107, 0.2-0.5 pH unit accuracy) digital pH meter. The extent of mineralization was determined using a total organic carbon analyzer (TOC - Shimadzu VCPN). The PCD efficiency ( $\eta$ ) was calculated from the following expression,  $\eta = C_i - C_t / C_i \times 100$  (or)  $\eta = \text{TOC}_i - \text{TOC}_t / \text{TOC}_i \times 100$ , where,  $C_i$  or  $\text{TOC}_i$ , initial concentration of 4-CP,  $C_t$  or  $\text{TOC}_t$ , concentration of 4-CP after 't' minutes.

### 3. Results and discussion

#### 3.1. Structural analysis

The structural phase and purity of the as-prepared Mn<sub>x</sub>Zn<sub>1-x</sub>Fe<sub>2</sub>O<sub>4</sub> NCs were confirmed by analyzing the X-ray powder diffraction (XRD) patterns. Fig. 1 shows the XRD patterns of Mn<sub>x</sub>Zn<sub>1-x</sub>Fe<sub>2</sub>O<sub>4</sub> NCs prepared with various Mn substitutions ( $x = 0.0, 0.1, 0.2, 0.3, 0.4$  and  $0.5$ ). The main diffraction peaks ( $2\theta$ ) appear at about 29.76, 35.73, 36.92, 42.72, 53.16, 57.04, 62.13, 71.02, 74.14 and 78.83°, which are attributed to the (220), (311), (222), (400), (422), (511), (440), (620), (533) and (444) planes, respectively show the characteristics of a single-phase cubic

spinel structure with Fd3m space group (JCPDS card no. 22-1012) [37]. The observed diffraction peaks indicates well defined spinel phase, which was developed during the combustion. During the heating process, naturally oxidation and formation of metal oxide is very common. Moreover, the control of furnace atmosphere during complete combustion is also very crucial. However, some peaks of  $\alpha$ -Fe<sub>2</sub>O<sub>3</sub> phase can also be observed at  $2\theta = 24.02$  and  $42.12^\circ$  in each diffraction pattern, it is mainly due to the partial oxidation of ZnFe<sub>2</sub>O<sub>4</sub> and Mn-Zn ferrites [38]. The main diffraction peak of cubic spinel ferrite at (311) plane was considered as a measure of its degree of crystallinity.

The average crystallite size of the as-prepared NCs was calculated from the diffraction peak of the (311) plane in the XRD profile, in accordance with Debye-Scherrer formula:

$$L = \frac{0.89\lambda}{\beta \cos \theta}$$

where ' $L$ ' is the average crystallite size, ' $\lambda$ ', the X-ray wavelength (0.1542 nm), ' $\beta$ ', full width at half maximum (FWHM) and ' $\theta$ ', the Bragg angle of the (311) plane. The calculated crystallite size of the samples is summarized in Table 1. It has been observed that the crystallite size is decreased from 23.25-17.53 nm with increase in Mn content, upto  $x = 0.0$ - $0.3$ . However, and further increase the Mn content ( $x = 0.4$  and  $0.5$ ) the crystallite size is decreased from 17.92-18.36 nm. It has a minimum crystallite size of 17.53 nm for 0.3 Mn content (Mn<sub>0.3</sub>Zn<sub>0.7</sub>Fe<sub>2</sub>O<sub>4</sub>). The results show a significant amount of XRD line broadening, a characteristic of nano-phase materials.

In order to further analyze the structural change, the measured XRD patterns of the NCs were simulated based on the Rietveld refinement method. Rietveld XRD data analysis of the as-

prepared NCs is shown in Fig. 2. It was designed to refine simultaneously both the structural and microstructural parameters (Lattice constant and Crystallite size). During the refinements, the goodness of fit is defined by the reliability factor  $S = R_{wp}/R_e$ , where  $R_{wp}$  and  $R_e$ , are, respectively, the  $R_{wp}$ -weighted and the  $R_e$ -expected patterns. The obtained values of the lattice parameter and crystallite size from the Rietveld analysis are shown in Fig. 3 and Table 1. The lattice parameter of pure  $ZnFe_2O_4$  is found to be equal to  $8.442 \text{ \AA}$ , which is in good accordance with the standard value of  $8.441 \text{ \AA}$  (JCPDS No. 22-1012). The lattice parameter increases with increasing Mn content from  $8.442$  to  $8.451 \text{ \AA}$ , thus obeying Vegard's law. The Vegard's law is based on the change due to ionic radii of replacing and replaced ions and predicts the linear change in the lattice parameter for the spinel system with the substitution of different ions. The ionic radius of  $Mn^{2+}$  ion ( $0.91 \text{ \AA}$ ) is higher than that of  $Zn^{2+}$  ion ( $0.82 \text{ \AA}$ ), and thus causes an effective increase in the lattice constant. A linear increase in the lattice constant thus indicates that the Mn ions are replacing the Zn ions in  $ZnFe_2O_4$  matrix and also confirms that Mn is occupied in the lattice of spinel ferrite [39, 40].

### 3.2. Fourier transform infrared (FT-IR) spectroscopy

Fourier transform infrared (FT-IR) spectra were recorded on a Perkin Elmer FT-IR spectrometer using the KBr pellet method. FT-IR spectra of  $Mn_xZn_{1-x}Fe_2O_4$  ( $x = 0.0, 0.1, 0.2, 0.3, 0.4$  and  $0.5$ ) nano-crystals are shown in Fig. 4. From the FT-IR spectra, it is found that two strong absorption peaks observed at lower frequency ( $825$  and  $430 \text{ cm}^{-1}$ ) can be assigned to the M-O (Zn, Mn and Fe) bonds at A and B sites [27, 41]. This can be attributed to the high degree of crystalline nature of the  $Mn_xZn_{1-x}Fe_2O_4$  nano-crystals. The obtained results were good agreement with Rietveld refinement XRD analysis. A broad vibration band at  $\sim 3440 \text{ cm}^{-1}$  is

associated with the OH stretching vibrations of water molecules, indicating higher amount of surface hydroxyl groups (OH), while those at  $\sim 1630\text{ cm}^{-1}$  are associated with their bending mode. Generally, the  $\text{H}_2\text{O}$  and  $\text{CO}_2$  molecules are easily chemisorbed onto  $\text{Mn}_x\text{Zn}_{1-x}\text{Fe}_2\text{O}_4$  nanocrystals surface when exposed to the atmosphere. However, in this present study, we have observed two bands at  $\sim 825$  and  $\sim 430\text{ cm}^{-1}$  was confirmed the M-O (Zn, Mn and Fe) bonds stretching vibrations in A- and B- sites of magnetic spinel  $\text{Mn}_x\text{Zn}_{1-x}\text{Fe}_2\text{O}_4$  NCs. Similar values are reported earlier [27, 41, 42].

### 3.3. Scanning electron microscopy (SEM) studies

The morphological characteristics of the spinel  $\text{Mn}_x\text{Zn}_{1-x}\text{Fe}_2\text{O}_4$  NCs were investigated by the high resolution scanning electron microscopy (HR-SEM) and the obtained results are shown in Fig. 5. Fig. 5a-c shows the HR-SEM images of pure  $\text{ZnFe}_2\text{O}_4$ ,  $\text{Mn}_{0.3}\text{Zn}_{0.7}\text{Fe}_2\text{O}_4$  and  $\text{Mn}_{0.5}\text{Zn}_{0.5}\text{Fe}_2\text{O}_4$  samples, respectively. HR-SEM images indicated that the as-prepared samples consist of well crystallized homogeneous spherical shaped particle-like nanocrystals, which are agglomerated together, due to the presence of magnetic interactions among the particles [43].

### 3.4. Transmission electron microscopy (TEM) studies

To provide a further evidence for the formation of spherical shaped particle-like nanocrystal morphology of the as-synthesized  $\text{Zn}_{1-x}\text{Mn}_x\text{Fe}_2\text{O}_4$  samples, high resolution transmission electron microscopy (HR-TEM) analysis was carried out and is shown in Fig. 6. Fig. 6a shows the HR-TEM image of undoped  $\text{ZnFe}_2\text{O}_4$  particle-like nanocrystals with diameter ranging from 23-25 nm. Fig. 6b,c shows the HR-TEM images of  $\text{Mn}_{0.3}\text{Zn}_{0.7}\text{Fe}_2\text{O}_4$  and  $\text{Mn}_{0.5}\text{Zn}_{0.5}\text{Fe}_2\text{O}_4$  NCs, respectively, with diameter ranging from 15-21 nm. It is obvious that the spherical shaped particle-like nano-crystals are uniform in size, which is consistent with the average crystallite

size obtained from the peak broadening in XRD and Rietveld analysis. The observed average particle size is close to the values obtained using the Scherer equation. The nano-sized features are noticeably visible in Fig. 6a-c, which was found to be highly crystalline as evident from HR-TEM image displayed in Fig. 6d. Fig. 6d yields an inter-planar distance  $d$  spacing of 0.25 nm can be assigned to the (311) lattice plane of the cubic spinel  $\text{ZnFe}_2\text{O}_4$  nanocrystals [44]. It clearly showed that the nano-crystals are agglomerated, due to the presence of the magnetic interactions among the particles. Selected area electron diffraction pattern (SAED) of  $\text{ZnFe}_2\text{O}_4$  nano-crystals are shown in Fig. 6a (inset), which implies that the as-prepared samples are single crystalline in nature.

### 3.5. Energy dispersive X-ray (EDX) analysis

The elemental composition and purity of the as-prepared nanocrystals were recorded at room temperature by EDX analysis. Fig. 7 shows the EDX results of pure and  $\text{Mn}^{2+}$ -doped  $\text{ZnFe}_2\text{O}_4$  ( $\text{Mn}_x\text{Zn}_{1-x}\text{Fe}_2\text{O}_4$ :  $x = 0.0$  and  $0.5$ ) nano-crystals. Fig. 7a shows the peaks of Fe, Zn and O elements in pure  $\text{ZnFe}_2\text{O}_4$  and Fig. 7b, shows the peaks of Fe, Zn, Mn and O elements for Mn-doped  $\text{ZnFe}_2\text{O}_4$  samples, and there is no other peaks, which is confirmed the as-prepared samples are pure and there is no other impurity. The above mentioned results confirm the formation of pure and Mn-doped  $\text{ZnFe}_2\text{O}_4$  phase. The percentage of Mn/Zn values obtained is given in the inset of Fig. 7a, b. Pure  $\text{ZnFe}_2\text{O}_4$  and Mn-doped  $\text{ZnFe}_2\text{O}_4$  did not deviate from their initial stoichiometry and matched well with the initial degree of  $\text{Mn}^{2+}$  substitutions in  $\text{ZnFe}_2\text{O}_4$  spinel. It is interesting to note that the urea-assisted auto combustion method completely favors the formation of spinel  $\text{ZnFe}_2\text{O}_4$ . A small peak was appeared at 2.1 KeV for all the samples, which

indicated the presence of Au (gold) peak that has been used as a sputter coating, while preparing the sample for HR-SEM analysis for the better visibility of the surface morphology.

### 3.6. Diffuse reflectance spectroscopy (DRS) studies

To study the effect of crystallite size and crystallinity on the optical properties of spinel  $\text{ZnFe}_2\text{O}_4$  semiconductor materials, the UV-Visible diffuse reflectance spectroscopy (DRS) measurement was carried out at room temperature for all compositions. The band gap energy  $E_g$ , can be approximately calculated from the optical diffuse reflectance data by the Kubelka-Munk function,  $F(R) = (1-R)^2 / 2R$ , where 'R' is the diffuse reflectance. A graph is plotted between  $[F(R)h\nu]^2$  and  $h\nu$ , and the intercept obtained is the band gap energy (Fig. 8a). The estimated band gap ( $E_g$ ) values of  $\text{Mn}_x\text{Zn}_{1-x}\text{Fe}_2\text{O}_4$  ( $x = 0.0, 0.1, 0.2, 0.3, 0.4$  and  $0.5$ ) nano-crystals are 1.95, 2.01, 2.18, 2.27, 2.31, and 2.40 eV, respectively (Fig.8b and Table 1). It clearly shows that there is increase in the band gap energy of  $\text{Mn}^{2+}$ -doped  $\text{ZnFe}_2\text{O}_4$  samples, when compared to the undoped  $\text{ZnFe}_2\text{O}_4$  nanoparticles ( $E_g = 1.95$  eV). This is mainly attributed to the reduction in size of  $\text{ZnFe}_2\text{O}_4$  NCs (Quantum confinement effect) as Mn content increase. Thus, the use of size quantized doped semiconductor materials may result in increased photocatalytic activity. The band-gap ( $E_g$ ) value of bulk  $\text{ZnFe}_2\text{O}_4$  is 1.9 eV, and hence there is a blue shift for all compositions. This may be due to the additional sub-band-gap energy levels that are induced by the abundant surface and interface defects in the agglomerated nano-crystals [45]. The shift in  $E_g$  of the  $\text{Mn}_x\text{Zn}_{1-x}\text{Fe}_2\text{O}_4$  nano-crystals with the decreasing crystallite size is the result of quantum confinement effects arising from the small size regime [46]. Similar results were reported in other literatures, in which the values of the band gap energy given are 1.9 and 2.23 eV [29, 47].

Fan et al. reported similar band gaps (2.1, 2.0 and 1.9 eV) for pure  $\text{ZnFe}_2\text{O}_4$  with three different ranges of particle sizes [48].

However, the band gap values are increases with increase in the concentration of  $\text{Mn}^{2+}$  content. The band gap values are affected by various factors, such as particle size, crystallinity, structural parameter (lattice constant), nature and composition of impurities (dopant). The increase in the band gap of our synthesized  $\text{Mn}_x\text{Zn}_{1-x}\text{Fe}_2\text{O}_4$  ( $x = 0.0, 0.1, 0.2, 0.3, 0.4$  and  $0.5$ ) nano-crystals may be attributed to the more increase in the structural parameter (lattice constant) with the increase in the Mn content in comparison to the undoped  $\text{ZnFe}_2\text{O}_4$  (Tables 1). Moreover, the obtained band gap values of pure and Mn-doped  $\text{ZnFe}_2\text{O}_4$  nano-crystals are higher than that of bulk (1.9 eV) and estimated band gap values of zinc ferrite nanowires [47], which are 2.23 and 1.73 eV, respectively, and are similar to the  $\text{ZnFe}_2\text{O}_4$  films [49]. The band gap energy of the nano-crystals increases with decrease in the particle size, due to the quantum confinement effect.

### ***3.7. Photoluminescence (PL) studies***

The photoluminescence (PL) spectroscopy technique have been widely used to examine the structure and properties of the active sites on the surface of metal oxides. PL spectrum is an effective approach to study the electronic structure, optical and photochemical properties of semiconductor materials. From the PL spectrum, one can obtain the information such as surface oxygen vacancies and defects, as well as the efficiency of the charge carrier trapping, immigration and transfer. The relationship between the PL spectrum and photochemical activity can be explained based on the PL phenomena of excited energy higher or equal to the band gap energy of semiconductor [50, 51].

Photoluminescence (PL) spectra was recorded at room temperature to detect the optical properties of  $\text{Mn}_x\text{Zn}_{1-x}\text{Fe}_2\text{O}_4$  nanostructures for various substitutions of  $\text{Mn}^{2+}$  ions ( $x = 0.0, 0.1, 0.2, 0.3, 0.4$  and  $0.5$ ) and are shown in Fig. 9a,b. All the samples were excited by using the excitation wavelength at 410 nm and the PL spectra shows the characteristic near-band-edge (NBE) emission at around 428 nm. The broadband visible emission band was observed in the entire PL spectrum at around 428 nm can be assigned to intrinsic defects, mainly interstitial zinc defects, and is attributed to the recombination of electrons deeply trapped in oxygen vacancies with photo-generated holes [52]. Spinel  $\text{ZnFe}_2\text{O}_4$  has been known to have the strong absorption in the UV-Visible range. As we increase the concentration of  $\text{Mn}^{2+}$  dopant into  $\text{ZnFe}_2\text{O}_4$ , overall intensities of the PL peak for all compositions decreases ( $x = 0.1, 0.2, 0.3, 0.4$  and  $0.5$ ). This may be explained as follows: (i) With increase in the  $\text{Mn}^{2+}$  concentration and leaving of the  $\text{Zn}^{2+}$  cations in the spinel structure,  $\text{Mn}^{2+}$  ions occupy the A- sites and transfer the  $\text{Fe}^{3+}$  to the B- sites. (ii) These changes cause a decrease in the structural isotropy of the as-synthesized nanoparticles. (iii) The sample  $\text{Mn}_{0.5}\text{Zn}_{0.5}\text{Fe}_2\text{O}_4$  NCs have biggest saturation magnetization ( $M_s$ ) than other samples and have a structural isotropy in the A- sites. (iv) The occupation of half of the A- sites by the  $\text{Mn}^{2+}$  ions and the rest by the  $\text{Fe}^{3+}$  ions causes the decrease in transitions of the  $\text{Fe}^{3+}$  ions in the A- sites. However, there are two minor peaks detected by the PL spectrometer at around 485 and 580 nm, for  $\text{Mn}_x\text{Zn}_{1-x}\text{Fe}_2\text{O}_4$  NCs respectively. However, the PL intensity of the emission bands at 428 nm is increases with the increase in the  $\text{Mn}^{2+}$  substitution in  $\text{ZnFe}_2\text{O}_4$ . This can be attributed to the appearance of new electronic levels between the conduction and the valence band and might be due to the increase in intrinsic defects. Thus, the employed urea-assisted one-pot combustion method can produce plenty of defects in pure  $\text{ZnFe}_2\text{O}_4$  and  $\text{Mn}^{2+}$  doped  $\text{ZnFe}_2\text{O}_4$

NCs. All the PL emission bands were slightly blue shifted and also broadened with higher PL intensity (Fig. 9b), due to the increase in Mn content. This can be attributed to the increased concreteness of surface defects, because of the presence of Mn dopants. Therefore, the band gap and PL of  $\text{ZnFe}_2\text{O}_4$  NCs can be manipulated by controlling their particle size and doping with metal ions, thus signify the capabilities of these nanostructures for assorted applications in various fields.

### 3.8 Magnetic measurements

Nano-structured spinel  $\text{Mn}_x\text{Zn}_{1-x}\text{Fe}_2\text{O}_4$  ( $x = 0.0, 0.1, 0.2, 0.3, 0.4$  and  $0.5$ ) photocatalyst exhibited typical magnetic behavior. The hysteresis loop (M-H curve) for  $\text{Mn}_x\text{Zn}_{1-x}\text{Fe}_2\text{O}_4$  nanocrystals are shown in Fig. 10, which clearly indicated that the prepared  $\text{Mn}_x\text{Zn}_{1-x}\text{Fe}_2\text{O}_4$  based photocatalyst can be separated from water by the application of external magnetic field. Furthermore, the as-prepared photocatalyst can be redispersed into water after eliminating the applied magnetic field (Fig. 10 inset). These magnetically responsive photocatalysts have main advantage over the conventional photocatalysts, because they can be recovered and recycled readily. Similar values are reported earlier by Shahid et al. [53].

The magnetic hysteresis (M-H) curves of the as-prepared  $\text{Mn}_x\text{Zn}_{1-x}\text{Fe}_2\text{O}_4$  ( $x = 0.0, 0.1, 0.2, 0.3, 0.4$  and  $0.5$ ) nanocrystals obtained from room temperature VSM measurement with the applied field ranging from  $-10000$  to  $+10000$  Oe is shown in Fig. 10. From the VSM measurements, saturation magnetization ( $M_s$ ), remanent magnetization ( $M_r$ ) and coercivity ( $H_c$ ) values are evaluated and are reported in Table 2. These curves are typical for a soft magnetic material and indicate hysteresis ferromagnetism in the field ranges of  $\pm 10$  KOe for the  $\text{Mn}_{0.3}\text{Zn}_{0.7}\text{Fe}_2\text{O}_4$ ,  $\text{Mn}_{0.4}\text{Zn}_{0.6}\text{Fe}_2\text{O}_4$  and  $\text{Mn}_{0.5}\text{Zn}_{0.5}\text{Fe}_2\text{O}_4$  respectively, whereas the samples of

ZnFe<sub>2</sub>O<sub>4</sub>, Mn<sub>0.1</sub>Zn<sub>0.9</sub>Fe<sub>2</sub>O<sub>4</sub> and Mn<sub>0.2</sub>Zn<sub>0.8</sub>Fe<sub>2</sub>O<sub>4</sub> show a superparamagnetic behavior. ZnFe<sub>2</sub>O<sub>4</sub> is a soft magnetic material. When non-magnetic Zn<sup>2+</sup> in ZnFe<sub>2</sub>O<sub>4</sub> is substituted by magnetic Mn<sup>2+</sup> ions, there is a drastic change in magnetic properties such as M<sub>s</sub>, M<sub>r</sub> and H<sub>c</sub>. Outside these ranges the value of M<sub>s</sub> increases with increasing the concentration of Mn<sup>2+</sup>. The values M<sub>s</sub> were obtained to be 6.928±03, 24.33±08, 37.77±15, 45.17±13, 55.24±02 and 67.38±11 emu/g at ±10 kOe for the samples of ZnFe<sub>2</sub>O<sub>4</sub>, Mn<sub>0.1</sub>Zn<sub>0.9</sub>Fe<sub>2</sub>O<sub>4</sub>, Mn<sub>0.2</sub>Zn<sub>0.8</sub>Fe<sub>2</sub>O<sub>4</sub>, Mn<sub>0.3</sub>Zn<sub>0.7</sub>Fe<sub>2</sub>O<sub>4</sub>, Mn<sub>0.4</sub>Zn<sub>0.6</sub>Fe<sub>2</sub>O<sub>4</sub> and Mn<sub>0.5</sub>Zn<sub>0.5</sub>Fe<sub>2</sub>O<sub>4</sub>, respectively. From the results, it is clearly understood that the magnetic properties of the samples are affected by the composition, cation distribution and nature of dopant [54].

However, the paramagnetic behavior of ZnFe<sub>2</sub>O<sub>4</sub> was observed in bulk [55] and nanoparticles [56]. In the case of undoped ZnFe<sub>2</sub>O<sub>4</sub> present a superparamagnetic behavior, which is due to the increase of anomalous Fe<sup>3+</sup> cation distribution in the A- sites upon nanosizing [57]. It can be seen that the M<sub>s</sub> values of spinel ferrites in this work are difference from those prepared by other methods. The difference of the magnetic properties in general depends on particle size, crystallinity, nature and composition of the dopant, magnetization direction, and so on. Also, these results point to that the magnetic properties of spinel ferrites are related to their preparation methods. However, hysteresis curve showed a typical superparamagnetic behavior of the as-prepared pure ZnFe<sub>2</sub>O<sub>4</sub>, Mn<sub>0.1</sub>Zn<sub>0.9</sub>Fe<sub>2</sub>O<sub>4</sub> and Mn<sub>0.2</sub>Zn<sub>0.8</sub>Fe<sub>2</sub>O<sub>4</sub> nanocrystals with lower remanance and coercivity. The absence of ferromagnetism of the above nanocrystals may be due to the non-equilibrium distribution of Fe<sup>3+</sup> ions in A- and B- sites. The non-saturation observed in M-H loop and the absence of the hysteresis, lower values of M<sub>r</sub> and H<sub>c</sub> indicates the superparamagnetic nature of the ferrite nanocrystals, which relax back their spins by rotation on

removal of applied magnetic field so as to give a zero net magnetic moment. The smaller value of  $M_s$  may be due to lattice defects, weaker magnetic super exchange interaction between A- and B- sites and random orientation of spin on the surface of nanocrystals [58]. For  $Mn_{0.3}Zn_{0.7}Fe_2O_4$ ,  $Mn_{0.4}Zn_{0.6}Fe_2O_4$  and  $Mn_{0.5}Zn_{0.5}Fe_2O_4$  nanocrystals, a hysteresis was observed, thus indicating the ferromagnetism. This is due to the increase in the magnetic nature of the  $Mn^{2+}$  concentration. The change in the value of  $M_s$  is most probably due to the difference in the cation sharing at the A- and B- sites.

The cation distribution of Mn-Zn ferrite is  $[Zn^{2+}_{1-x}Fe^{3+}_{1+x}]_A [Mn^{2+}_xFe^{3+}_{1-x}]_B O_4^{2-}$ ; where the term within the square brackets indicates the tetrahedral (A-) and octahedral (B-) sites.  $Mn^{2+}$  ions have a tendency to go into the B-sites in the crystal lattice, because of the favorable fit of charge distribution of this ion in the crystal field of the B- site. On other hand,  $Zn^{2+}$  ions have a preference for the A- site, due to their readiness to form covalent bonds involving  $sp^3$  hybrid orbitals [59]. However, the non-magnetic  $Zn^{2+}$  (0  $\mu B$ ) are replaced by the magnetic  $Mn^{2+}$  (5  $\mu B$ ) ions, which increase the  $M_s$  when, the magnetic  $Mn^{2+}$  ions introduced in the lattice, it starts to occupy the B- sites and replace  $Fe^{3+}$  ions from the B- sites, which then start migrating towards the A- sites. Therefore,  $Fe^{3+}$  ions partially occupy the A- and B- sites [60]. The weakening of A-B exchange coupling, due to this migration results in the increase in magnetic moment.

The value of  $M_s$  for pure  $ZnFe_2O_4$  is  $6.928 \pm 03$  emu/g, which increases with the increase in  $Mn^{2+}$  concentration ( $x = 0.1-0.5$ ,  $M_s = 24.33 \pm 08$  to  $67.38 \pm 11$  emu/g). Kumar et al. [61] reported magnetic nature of  $Ni^{2+}$  ion doped zinc ferrite ( $Ni_xZn_{1-x}Fe_2O_4$  where  $x = 0.1, 0.3, 0.5$ ) nanoparticles synthesized by a chemical co-precipitation method. They reported the doping effect of  $Ni^{2+}$  ions on the  $M_s$  and the values are increased (23.95 to 37.75 emu/g) with increasing

Ni content ( $x = 0.1-0.5$ ). Koseoglu et al. [62] reported the  $M_s$  value of 5 emu/g for  $ZnFe_2O_4$  magnetic nanoparticles prepared by a PEG-assisted route.

Moreover, the  $M_s$  values of the as-prepared  $ZnFe_2O_4$  samples is smaller than that observed for the bulk  $ZnFe_2O_4$  (70 emu/g) [63]. These differences in the  $M_s$  values between the nanoferrites and bulk ferrites, which can be attributed to the finite size effects [64]. Also, the magneto-crystalline anisotropy of the particles is dependent on the crystallinity of the nanocrystals. In this present auto combustion method, the nanocrystals are prepared at lower temperatures (400 °C/2h), and it has produced moderately crystallized particles. Therefore, a large amount of crystal defects can occur within the spinel lattice, and will cause a considerable reduction of magnetic moment inside the particles, as a result of the magnetocrystalline anisotropy distortion. Also, the very low values of  $H_c$  and  $M_r$ , indicate that they are also soft magnets.

### ***3.9 Photocatalytic properties***

It has been usually accepted that the crystallinity, particle size, concentrations of doping metal ions and morphologies of the nano-materials are significant factors that influence its photocatalytic performance. Li et al. [65] have previously reported that photocatalytic activity of  $ZnFe_2O_4$  nanostructures mainly determined by its particle morphology. Jia et al. [66] reported that the photocatalytic activity of porous  $ZnFe_2O_4$  nanostructures obviously relies on surface properties and surface defects. Therefore, it is important to prepare  $Mn_xZn_{1-x}Fe_2O_4-TiO_2$  ( $0.0 \leq x \leq 0.5$ ) NCs and understand the chemistry occurring at  $TiO_2$  supported in  $Mn_xZn_{1-x}Fe_2O_4$  ( $0.0 \leq x \leq 0.5$ ) NCs surface in order to control and tune the photocatalytic properties of the pure and Mn-doped  $ZnFe_2O_4$  NCs. Hence, undoped  $ZnFe_2O_4-TiO_2$  and Mn doped  $ZnFe_2O_4-TiO_2$  NCs surface

characterization and the correlation of structure with observed photocatalytic properties remains important. Thus, we made an attempt to reveal the relationship between optical and photocatalytic properties of pure metal oxides ( $\text{ZnFe}_2\text{O}_4$  and  $\text{TiO}_2$ ) and Mn doped mixed metal oxides of  $\text{ZnFe}_2\text{O}_4\text{-TiO}_2$  ( $\text{Mn}_{0.1}\text{Zn}_{0.9}\text{Fe}_2\text{O}_4\text{-TiO}_2$ ,  $\text{Mn}_{0.2}\text{Zn}_{0.8}\text{Fe}_2\text{O}_4\text{-TiO}_2$ ,  $\text{Mn}_{0.3}\text{Zn}_{0.7}\text{Fe}_2\text{O}_4\text{-TiO}_2$ ,  $\text{Mn}_{0.4}\text{Zn}_{0.6}\text{Fe}_2\text{O}_4\text{-TiO}_2$  and  $\text{Mn}_{0.5}\text{Zn}_{0.5}\text{Fe}_2\text{O}_4\text{-TiO}_2$ ) NCs and a series of experiments were carried out with 4-CP in aqueous suspension with the light of wavelength 365 nm.

### ***3.9.1 Effects of $\text{TiO}_2$ supported and Mn doping on the photocatalytic activity of $\text{Mn}_x\text{Zn}_{1-x}\text{Fe}_2\text{O}_4$ ( $0.0 \leq x \leq 0.5$ ) NCs***

The influence of  $\text{TiO}_2$  supported and Mn doping on  $\text{ZnFe}_2\text{O}_4\text{-TiO}_2$  NCs on the PCD efficiency is evaluated as shown in Fig. 11. The PCD efficiency of pure  $\text{ZnFe}_2\text{O}_4$  is very low when compared with  $\text{TiO}_2$ . The PCD efficiency of  $\text{TiO}_2$  supported  $\text{ZnFe}_2\text{O}_4$  ( $\text{ZnFe}_2\text{O}_4\text{-TiO}_2$  NCs) is higher than pure  $\text{ZnFe}_2\text{O}_4$  NCs. However, the PCD efficiency of  $\text{Mn}_x\text{Zn}_{1-x}\text{Fe}_2\text{O}_4\text{-TiO}_2$  ( $0.0 \leq x \leq 0.5$ ) NCs increases with an increase in the concentration of Mn loading and showed a maximum activity at  $x = 0.3$  ( $\text{Mn}_{0.3}\text{Zn}_{0.7}\text{Fe}_2\text{O}_4\text{-TiO}_2$ ) and then decreases on further Mn doping to  $x = 0.5$  ( $\text{Mn}_{0.5}\text{Zn}_{0.5}\text{Fe}_2\text{O}_4\text{-TiO}_2$ ). The reason can be explained as follows: As smaller particle size distribution of  $\text{Mn}_{0.3}\text{Zn}_{0.7}\text{Fe}_2\text{O}_4\text{-TiO}_2$  NCs, more surface defects are produced as demonstrated in PL spectra, and a space charge layer could be formed on the surface. Therefore, the migration of the photo-induced electrons and holes toward surface defects is sensible [67]. Hence, the separation efficiency of the electron-hole pairs of  $\text{Mn}_{0.3}\text{Zn}_{0.7}\text{Fe}_2\text{O}_4\text{-TiO}_2$  NCs with more oxygen defects should be more than that of  $\text{ZnFe}_2\text{O}_4\text{-TiO}_2$  NCs. Therefore, the improvement in the PCD efficiency of  $\text{ZnFe}_2\text{O}_4\text{-TiO}_2$  NCs as Mn doping increases was recognized to the small particle size and higher defect application. Nevertheless, excessive amounts of Mn-dopants ( $x = 0.4$  and

0.5) can retard the photocatalysis process, because excess amount of dopants deposited on the surface of  $\text{ZnFe}_2\text{O}_4\text{-TiO}_2$  increases the recombination rate of free electrons and energetic holes, thus inhibiting the photo-degradation process. Hence, further increase in Mn doping ( $x = 0.5$ ), results in the decrease of PCD efficiency. However, the sample  $\text{Mn}_{0.3}\text{Zn}_{0.7}\text{Fe}_2\text{O}_4\text{-TiO}_2$  NCs shows maximum activity for 4-CP photo-degradation, which is attributed to a gradual crystallization of zinc ferrite and further increase in the  $\text{Mn}^{2+}$  doping results in an obvious decrease in activity, which is due to the increase of the grain size [68].

However, in our present study shows that the photocatalytic activity of single phase  $\text{ZnFe}_2\text{O}_4$  is enhanced, when it is coupled with  $\text{TiO}_2$  to form a composite catalyst and it is further enhanced when an addition of Mn is present in the  $\text{Mn}_x\text{Zn}_{1-x}\text{Fe}_2\text{O}_4\text{-TiO}_2$  composite catalyst. Though, the band gap of  $\text{ZnFe}_2\text{O}_4$  is smaller than that of  $\text{TiO}_2$  and it is a visible light active catalyst, it exhibits lower photocatalytic activity, due to its lower valence band potential compared to  $\text{TiO}_2$ . When  $\text{TiO}_2$  and  $\text{ZnFe}_2\text{O}_4$  are coupled and irradiated with UV-Vis light, the photocatalytic activity is improved, though the charge carriers can migrate to  $\text{ZnFe}_2\text{O}_4$ , due to the higher VB potential of  $\text{TiO}_2$ . The increased activity of the composite, when Mn is present is due to the decrease in the migration of the charge carriers from  $\text{TiO}_2$  to  $\text{ZnFe}_2\text{O}_4$ .

### ***3.9.2 Effect of surface area on the photocatalytic activity***

In order to have an idea of the adsorbance capability of the nanocrystals, BET surface area analysis was determined using  $\text{N}_2$  adsorption/desorption studies. BET surface areas of  $\text{ZnFe}_2\text{O}_4$ ,  $\text{TiO}_2$ ,  $\text{ZnFe}_2\text{O}_4\text{-TiO}_2$ ,  $\text{Mn}_{0.1}\text{Zn}_{0.9}\text{Fe}_2\text{O}_4\text{-TiO}_2$ ,  $\text{Mn}_{0.2}\text{Zn}_{0.8}\text{Fe}_2\text{O}_4\text{-TiO}_2$ ,  $\text{Mn}_{0.3}\text{Zn}_{0.7}\text{Fe}_2\text{O}_4\text{-TiO}_2$ ,  $\text{Mn}_{0.4}\text{Zn}_{0.6}\text{Fe}_2\text{O}_4\text{-TiO}_2$  and  $\text{Mn}_{0.5}\text{Zn}_{0.5}\text{Fe}_2\text{O}_4\text{-TiO}_2$  nanocrystals are 37.25, 48.52, 42.47, 56.42, 61.69, 75.64, 73.26, and 72.16  $\text{m}^2/\text{g}$ , respectively. The surface area is increased with

increasing the concentration of Mn content ( $x = 0.3$ ) and the sample  $\text{Mn}_{0.3}\text{Zn}_{0.7}\text{Fe}_2\text{O}_4\text{-TiO}_2$  was found to be higher surface area ( $75.64 \text{ m}^2/\text{g}$ ) than other samples, and further increase the Mn content ( $x = 0.4$  and  $0.5$ ) the surface area decreased. Therefore, it is believed that the high surface area of  $\text{Mn}_{0.3}\text{Zn}_{0.7}\text{Fe}_2\text{O}_4\text{-TiO}_2$  NCs could enhance the photocatalytic properties than that of other samples (Fig. 11). The BET surface area and pore structure play an important role in improving catalyst performance.

In general, a high specific surface area has a favorable effect on the activity for photocatalysts. However, the photocatalytic performance is increases with increasing the surface area as shown in Fig. 11. It is found that the high specific surface area of  $\text{Mn}_{0.3}\text{Zn}_{0.7}\text{Fe}_2\text{O}_4\text{-TiO}_2$  NCs was beneficial to photocatalytic activity via attractive the adsorption of 4-CP, which is the determining step in the heterogeneous photocatalytic reaction. Usually, photocatalyst with a high specific surface area would offer more surface active sites and photocatalytic reaction centers, resulting in the enhancement of photocatalytic performance. Thus the higher surface area of  $\text{Mn}_{0.3}\text{Zn}_{0.7}\text{Fe}_2\text{O}_4\text{-TiO}_2$  NCs may lead to higher photocatalytic activity, as compared to other samples [69]. In addition, when the size of particles decreases, the amount of the dispersion of particles per volume in the solution will increase, which resulting the enhancement of the photon absorbance. Besides, as the particle size decreases, the number of active surface sites increases. Therefore, the photocatalytic activity of  $\text{Mn}_{0.3}\text{Zn}_{0.7}\text{Fe}_2\text{O}_4\text{-TiO}_2$  NCs is higher than other samples, due to that with very smaller particle size distribution would be a potentially efficient photocatalyst.

### ***3.9.3 Effect of phenol concentration on PCD efficiency***

The rate of photo-catalytic degradation of 4-CP was strongly depended on the initial concentration of 4-CP and it is found that the efficiency is decreased from 95.5% to 72.3% with the increase in the initial 4-CP concentration from 50 to 250 mg/L after 210 min (Fig. 12). This may be suitable to the fact that as the initial concentration of 4-CP increases, more and more 4-CP molecules are adsorbed on the surface of  $\text{Mn}_x\text{Zn}_{1-x}\text{Fe}_2\text{O}_4\text{-TiO}_2$  ( $0.0 \leq x \leq 0.5$ ) NCs photocatalyst, but the number of  $\cdot\text{OH}$  and  $\cdot\text{O}_2^-$  radicals formed on the surface of  $\text{Mn}_x\text{Zn}_{1-x}\text{Fe}_2\text{O}_4\text{-TiO}_2$  ( $0.0 \leq x \leq 0.5$ ) NCs and the irradiation time is constant. The reactive species ( $\cdot\text{OH}$  and  $\cdot\text{O}_2^-$ ) required for the degradation of the contaminant on the catalyst surface remains constant for a given light intensity, catalyst amount and duration of irradiation. Hence, the available  $\cdot\text{OH}$  radicals are scarce for the photocatalytic degradation pollutant at higher concentrations. Therefore, relative number of  $\cdot\text{OH}$  and  $\cdot\text{O}_2^-$  radicals available for attacking 4-CP molecules becomes less, and consequently, PCD efficiency decreases. Also, as the concentration of 4-CP increases, the photons get interrupted before they can reach the photocatalyst surface; hence, absorption of photons by the photocatalyst decreases, and consequently, the PCD efficiency reduces [70]. As a result, the phenol (4-CP) degradation rate decreases as the concentration increases [71].

#### ***3.9.4 Effect of the catalyst dosage***

Blank experiments were carried out without photocatalyst to examine the extent of degradation (Photolysis). There was no evidence of PCD of 4-CP in aqueous solution in the absence of  $\text{Mn}_x\text{Zn}_{1-x}\text{Fe}_2\text{O}_4\text{-TiO}_2$  ( $0.0 \leq x \leq 0.5$ ) NCs. When aqueous solution of 4-CP containing  $\text{ZnFe}_2\text{O}_4\text{-TiO}_2$  NCs was irradiated with UV light, PCD of 4-CP was observed. The PCD of 4-CP was found to increase with increase in the amount of  $\text{ZnFe}_2\text{O}_4\text{-TiO}_2$  NCs up to 30 mg/100 mL,

and further increase in ZnFe<sub>2</sub>O<sub>4</sub>-TiO<sub>2</sub> NCs photocatalyst amount showed negative effect as illustrated in Fig. 13. This may be due to that the increase in the amount of ZnFe<sub>2</sub>O<sub>4</sub>-TiO<sub>2</sub> NCs catalyst increases the number of active sites on the photocatalyst surface, which in turn increase the number of hydroxyl ( $\cdot\text{OH}$ ) and superoxide ( $\cdot\text{O}_2^-$ ) radicals to degrade 4-CP. When the concentration of ZnFe<sub>2</sub>O<sub>4</sub>-TiO<sub>2</sub> NCs catalyst increases above the optimum value, the degradation is decreases, due to the interception of the light by the suspension. Sun et al. [72] have reported that as the excess of catalyst (turbidity) prevent the illumination of light,  $\cdot\text{OH}$  radical, a primary oxidant in the photocatalytic system decreased and hence the efficiency of the degradation reduced. Furthermore, the increase in catalyst concentration beyond the optimum may result in the agglomeration of catalyst particles; hence, the part of the catalyst surface becomes unavailable for photon absorption, and thereby, PCD efficiency decreases [73]. In addition, an increase in the substrate concentration can lead to the production of the intermediates, which may adsorb on the surface of the catalyst. Unhurried distribution of the generated intermediates from the catalyst surface can effect in the deactivation of active sites on the photocatalyst and result in a reduction of the degradation rate.

Generally, 4-CP photocatalytic degradation was occurred by hydroxyl radicals attack at the phenyl group of 4-CP. Therefore, in the present study, the PCD of 4-CP is believed to be initiated through attacks by hydroxyl radicals at the phenyl group of 4-CP, which may result in the formation of mono hydroxylated or dihydroxylated 4-CP. This is followed by the cleavage of the two phenyl groups into intermediates. Finally, the mineralization to CO<sub>2</sub> would have occurred via oxidative processes involving the cleavage of intermediates to aliphatic acids as shown in Scheme 3. The proposed degradation path way is given in Scheme 3. In addition,

hydroquinone was the major intermediates when 4-CP was oxidized at pH 2 and 4, while no aromatic intermediates were detected at pH 8. This may be due to the fact that hydroquinone in acidic medium can exist in equilibrium with quinone as shown in the Scheme 3. Hence, the mineralization of hydroquinone by photocatalytic degradation at acidic pH is rather difficult [74]. However, the concentration of hydroquinone and chlorocatechol was low in the pH range of 5-9, implying that the large amounts of non-aromatic intermediates may be produced when 4-CP was photocatalytically degraded as reported earlier [75]. Therefore, PCD efficiency at pH 8 is reasonably high.

#### 4. Conclusions

In summary, high-crystalline self-assembled pure  $\text{ZnFe}_2\text{O}_4$  and  $\text{Mn}^{2+}$ -doped  $\text{ZnFe}_2\text{O}_4$  NCs have been successfully synthesized by a facile, low-cost, urea assisted auto-combustion route. It was found that the structural, morphological, optical and magnetic properties are sensitively dependent on the incorporation of  $\text{Mn}^{2+}$  ions in the  $\text{Zn}^{2+}$  lattice site. The present study, leads to enhance the photocatalytic activity of spinel  $\text{Mn}_x\text{Zn}_{1-x}\text{Fe}_2\text{O}_4$  with the addition of  $\text{TiO}_2$ .  $\text{Mn}_x\text{Zn}_{1-x}\text{Fe}_2\text{O}_4\text{-TiO}_2$  mixed oxide catalysts were tested for the photocatalytic degradation of 4-CP, and the sample  $\text{Mn}_{0.3}\text{Zn}_{0.7}\text{Fe}_2\text{O}_4\text{-TiO}_2$  mixed oxides showed activity that was comparable to the activity of pure  $\text{ZnFe}_2\text{O}_4$  and  $\text{TiO}_2$ . Addition of  $\text{TiO}_2$  in  $\text{Mn}_x\text{Zn}_{1-x}\text{Fe}_2\text{O}_4$  NCs, which enhances the photocatalytic degradation of 4-CP. The photocatalytic activity of  $\text{Mn}_{0.3}\text{Zn}_{0.7}\text{Fe}_2\text{O}_4\text{-TiO}_2$  NCs was higher than the other Mn-doped  $\text{ZnFe}_2\text{O}_4$ , pure  $\text{ZnFe}_2\text{O}_4$ , and commercial  $\text{TiO}_2$  (Degussa P-25) at 365 nm than 254 nm, due to the very smaller particle size distribution would be a potentially efficient photocatalyst and high crystallinity, and surface defects, which significantly influence on the enhanced photocatalytic activity.

## **Acknowledgement**

One of the authors, A. Manikandan is thankful to CSIR, New Delhi, for the award of Senior Research Fellowship (CSIR-SRF).

**References**

- [1] Z. Jia, D. Ren, Y. Liang, R. Zhu, A new strategy for the preparation of porous zinc ferrite nanorods with subsequently light-driven photo catalytic activity, *Mater. Lett.* 65 (2011) 3116-3119.
- [2] Q. A. Pankhurst, J. Connolly, S.K. Jones, J. Dobson, Applications of magnetic nanoparticles in biomedicine, *J. Phys. D: App. Phys.* 36 (2003) R167.
- [3] R. Jurgons, C. Seliger, A. Hilpert, L. Trahms, S. Odenbach, C. Alexiou, Drug loaded magnetic nanoparticles for cancer therapy, *J. Phys. Condens. Matter* 18 (2006) S2893-S2902.
- [4] D.S. Mathew, R.S. Juang, An overview of structure and magnetism of spinel ferrite nanoparticles and their synthesis in microemulsions, *Chem. Eng. J.* 129 (2007) 51-65.
- [5] K. Janghorban, H. Shokrollahi, Influence of  $V_2O_5$  addition on the grain growth and magnetic properties of Mn-Zn high permeability ferrites, *J. Magn. Magn. Mater.* 308 (2007) 238-242.
- [6] M. Srivastava, A.K. Ojha, S. Chaubey, A. Materny, Synthesis and optical characterization of nanocrystalline  $NiFe_2O_4$  structures, *J. Alloys Compd.* 481 (2009) 515-519.
- [7] I. H. Gul, A. Maqsood, Structural, magnetic and electrical properties of cobalt ferrites prepared by the sol-gel route, *J. Alloys Compd.* 465 (2008) 227-231.
- [8] Y. Koseoglu, A. Baykal, M.S. Toprak, F. Gozuak, A.C. Basaran, B. Akas, Synthesis and characterization of  $ZnFe_2O_4$  magnetic nanoparticles via a PEG-assisted route, *J. Alloys Compd.* 462 (2008) 209-213.
- [9] S.D. Jadhav, P.P. Hankare, R.P. Patil, R. Sasikala, Effect of sintering on photocatalytic degradation of methyl orange using zinc ferrite, *Mater. Lett.* 65 (2011) 371-373.

- [10] P.P. Hankare, R.P. Patil, A.V. Jadhav, K.M. Garadkar, R. Sasikala, Enhanced photocatalytic degradation of methyl red and thymol blue using titania-alumina-zinc ferrite nanocomposite, *App. Catal. B: Env.* 107 (2011) 333-339.
- [11] S. Sultana, Rafiuddin, M. Z. Khan, K. Umar, Synthesis and characterization of copper ferrite nanoparticles doped polyaniline, *J. Alloys Compd.* 535 (2012) 44-49.
- [12] D. Varshney, K. Verma, A. Kumar, Structural and vibrational properties of  $Zn_xMn_{1-x}Fe_2O_4$  ( $x = 0.0, 0.25, 0.50, 0.75, 1.0$ ) mixed ferrites, *Mater. Chem. Phys.* 131 (2011) 413-419.
- [13] H. H. Hamdeh, J.C. Ho, S.A. Oliver, R.J. Willey, G. Oliveri, G.J. Busca, Magnetic properties of partially-inverted zinc ferrite aerogel powders, *J. Appl. Phys.* 81 (1997) 1851-1857.
- [14] S. H. Yu, T. Fujino, M. Yoshimura, Hydrothermal synthesis of  $ZnFe_2O_4$  ultrafine particles with high magnetization, *J. Magn. Magn. Mater.* 256 (2003) 420-424.
- [15] M. Sivakumar, A. Towata, K. Yasui, T. Tuziuti, Y. Iida, A new ultrasonic cavitation approach for the synthesis of zinc ferrite nanocrystals, *Curr. Appl. Phys.* 6 (2006) 591-593.
- [16] C. Rath, S. Anand, R.P. Das, K.K. Sahu, S.D. Kulkarni, S.D. Date, N.C. Mishra, Dependence on cation distribution of particle size, lattice parameter, and magnetic properties in nanosize Mn-Zn ferrite, *J. Appl. Phys.* 91 (2002) 2211-2215.
- [17] E. Auzans, D. Zins, E. Blums, R. Massart, Synthesis and properties of Mn-Zn ferrite ferrofluids, *J. Mater. Sci.* 34 (1999) 1253-1260.
- [18] A. Azam, Microwave assisted synthesis and characterization of Co doped Cu ferrite nanoparticles, *J. Alloys Compd.* 540 (2012) 145-153.

- [19] A. Azam, A. Jawad, A.S. Ahmed, M. Chaman, A.H. Naqvi, Structural, optical and transport properties of  $\text{Al}^{3+}$  doped  $\text{BiFeO}_3$  nanopowder synthesized by solution combustion method, *J. Alloys Compd.* 509 (2011) 2909-2913.
- [20] F. Gozuak, Y. Koseoglu, A. Baykal, H. Kavas, Synthesis and characterization of  $\text{Co}_x\text{Zn}_{1-x}\text{Fe}_2\text{O}_4$  magnetic nanoparticles via PEG-assisted route, *J. Magn. Magn. Mater.* 321 (2009) 2170-2177.
- [21] Y. Koseoglu, Structural, magnetic, electrical and dielectric properties of  $\text{Mn}_x\text{Ni}_{1-x}\text{Fe}_2\text{O}_4$  spinel nanoferrites prepared by PEG assisted hydrothermal method, *Ceram. Int.* 39 (2013) 4221-4230.
- [22] S. S. Manoharan, N.R.S. Kumar, K.C. Patil, Preparation of fine particle chromates: A combustion approach, *Mat. Res. Bull.* 25 (1990) 731-738.
- [23] S. S. Manoharan, V. Prasad, S.V. Subramanyam, K.C. Patil, Combustion synthesis and properties of fine particle  $\text{La}_2\text{CuO}_4$  and  $\text{La}_{1.8}\text{Sr}_{0.2}\text{CuO}_4$ , *Physica C* 190 (1992) 225-228.
- [24] S. S. Manoharan, K.C. Patil, Combustion route to fine particle perovskite oxides, *J. Solid State Chem.* 102 (1993) 267-276.
- [25] C. Upadhjay, D. Mishra, H.C. Varma, S. Anand, R.P. Das, Effect of preparation conditions on formation of nanophase Ni-Zn ferrites through hydrothermal technique, *J. Magn. Magn. Mater.* 260 (2003) 188-194.
- [26] A. Feteira, Negative temperature coefficient resistance (NTCR) ceramic thermistors: An industrial perspective, *J. Am. Ceram. Soc.* 92 (2009) 967-983.

- [27] S. H. Xu, D. L. Feng, W. F. Shangguan, Preparations and photocatalytic properties of visible-light-active zinc ferrite-doped TiO<sub>2</sub> photocatalyst. *J. Phys. Chem. C* 113 (2009) 2463-2467.
- [28] G. Y. Zhang, Y. Q. Sun, D. Z. Gao, Y. Y. Xu, Quasi-cube ZnFe<sub>2</sub>O<sub>4</sub> nanocrystals: hydrothermal synthesis and photocatalytic activity with TiO<sub>2</sub> (Degussa P25) as nanocomposite. *Mater. Res. Bull.* 45 (2010) 755-760.
- [29] P. H. Borse, J. S. Jang, S. J. Hong and J. S. Lee, J. H. Jung, T. E. Hong, C. W. Ahn, E. D. Jeong, K. S. Hong, J. H. Yoon, H. G. Kim, Photocatalytic hydrogen generation from water-methanol mixtures using nanocrystalline ZnFe<sub>2</sub>O<sub>4</sub> under visible light irradiation, *J. Korean Phys. Soc.* 55 (2009) 1472-1477.
- [30] H. Zhang, R. Hou, Z.L. Lu, X. Duan, A novel magnetic nanocomposite involving anatase titania coating on silica-modified cobalt ferrite via lower temperature hydrolysis of a water-soluble titania precursor, *Mater. Res. Bull.* 44 (2009) 2000-2008.
- [31] Y.S. Chung, S.B. Park, D.W. Kang, Magnetically separable titania-coated nickel ferrite photocatalyst, *Mater. Chem. Phys.* 86 (2004) 375-381.
- [32] S.W. Lee, J. Drwiega, D. Mazyck, C.Y. Wu, W.M. Sigmund, Synthesis and characterization of hard magnetic composite photocatalyst-Barium ferrite/silica/titania, *Mater. Chem. Phys.* 96 (2006) 483-488.
- [33] Y. Fu, X. Wang, Magnetically separable ZnFe<sub>2</sub>O<sub>4</sub>-graphene catalyst and its high photocatalytic performance under visible light irradiation, *Ind. Eng. Chem. Res.* 50 (2011) 7210-7218.

- [34] P. Xiong, J. Zhu, X. Wang, Cadmium sulfide-ferrite nanocomposite as a magnetically recyclable photocatalyst with enhanced visible-light-driven photocatalytic activity and photostability, *Ind. Eng. Chem. Res.* 52 (2013) 17126-17133.
- [35] H. Yang, L. Guo, W. Yan, H. Liu, A novel composite photocatalyst for water splitting hydrogen production, *J. Power Sources* 159 (2006) 1305-1309.
- [36] X. Fu, L.A. Clark, Q. Yang, M.A. Anderson, The enhanced photocatalytic performance of titania-based binary metal oxides:  $\text{TiO}_2/\text{SiO}_2$ ,  $\text{TiO}_2/\text{ZrO}_2$ , *Environ. Sci. Technol.* 30 (1996) 647-653.
- [37] S. Phumying, S. Labuayai, E. Swatsitang, V. Amornkitbamrung, S. Maensiri, Nanocrystalline spinel ferrite ( $\text{MFe}_2\text{O}_4$ ,  $\text{M} = \text{Ni, Co, Mn, Mg, Zn}$ ) powders prepared by a simple aloe vera plant-extracted solution hydrothermal route, *Mater. Res. Bull.* 48 (2013) 2060-2065.
- [38] H. Waqas, A. H. Qureshi, K. Subhan, M. Shahzad, Nanograin Mn-Zn ferrite smart cores to miniaturize electronic devices, *Ceram. Int.* 38 (2012) 1235-1240.
- [39] T. Tangcharoen, A. Ruangphanit, W. Pecharapa, Structural and magnetic properties of nanocrystalline zinc-doped metal ferrites (metal = Ni; Mn; Cu) prepared by sol-gel combustion method, *Ceram. Int.* 39 (2013) S239-S243.
- [40] A. Zapata, G. Herrero, Effect of zinc concentration on the microstructure and relaxation frequency of Mn-Zn ferrites synthesized by solid state reaction, *Ceram. Int.* 39 (2013) 7853-7860.
- [41] G. L. Fan, Z. J. Gu, L. Yang, F. Li, Nanocrystalline zinc ferrite photocatalysts formed using the colloid mill and hydrothermal technique. *Chem. Eng. J.* 155 (2009) 534-541.

- [42] A. Shanmugavani, R. KalaiSelvan, S. Layek, C. Sanjeeviraja, Size dependent electrical and magnetic properties of  $\text{ZnFe}_2\text{O}_4$  nanoparticles synthesized by the combustion method: Comparison between aspartic acid and glycine as fuels, *J. Magn. Mater.* 354 (2014) 363-371.
- [43] S. Rahman, K. Nadeem, M. A. Rehman, M. Mumtaz, S. Naeem, I. L. Papst, Structural and magnetic properties of ZnMg-ferrite nanoparticles prepared using the co-precipitation method, *Ceram. Int.* 39 (2013) 5235-5239.
- [44] J.S. Jang, P.H. Borse, J.S. Lee, O.S. Jung, C.R. Cho, E.D. Jeong, M.G. Ha, M.S. Won, H.G. Kim, Synthesis of nanocrystalline  $\text{ZnFe}_2\text{O}_4$  by polymerized complex method for its visible light photocatalytic application: An efficient photo-oxidant, *Bull. Korean Chem. Soc.* 30 (2009) 1738-1742.
- [45] N. Kislova, S.S. Srinivasan, Y. Emirov, E.K. Stefanakos, Optical absorption red and blue shifts in  $\text{ZnFe}_2\text{O}_4$  nanoparticles, *Mater. Sci. Eng. B* 153 (2008) 70-77.
- [46] B. Liu and H. C. Zeng, Salt-assisted deposition of  $\text{SnO}_2$  on  $\alpha\text{-MoO}_3$  nanorods and fabrication of polycrystalline  $\text{SnO}_2$  nanotubes, *J. Phys. Chem. B* 108 (2004) 5867-5874.
- [47] D. Gao, Z. Shi, Y. Xu, J. Zhang, G. Yang, J. Zhang, X. Wang, D. Xue, Synthesis, magnetic anisotropy and optical properties of preferred oriented zinc ferrite nanowire arrays, *Nanoscale Res. Lett.* 5 (2010) 1289-1294.
- [48] G. Fan, Z. Gu, L. Yang, F. Li, Nanocrystalline zinc ferrite photocatalysts formed using the colloid mill and hydrothermal technique, *Chem. Eng. J.* 155 (2009) 534-541.
- [49] M. Sultan, R. Singh, Magnetic and optical properties of sputtered zinc ferrite thin films, *J. Appl. Phys.* 105, 07A512 (2009).

- [50] J.C. Yu, J.G. Yu, K.W. Ho, Z.T. Jiang, L.Z. Zhang, Effects of F<sup>-</sup> doping on the photocatalytic activity and microstructures of nanocrystalline TiO<sub>2</sub> powders, *Chem. Mater.* 14 (2002) 3808-3816.
- [51] C.F. Song, M.K. Lu, P. Yang, D. Xu, D.R. Yuan, Structure and photoluminescence properties of sol-gel TiO<sub>2</sub>-SiO<sub>2</sub> films, *Thin Solid Films* 413 (2002) 155-159.
- [52] A.K. Srivastava, M. Deepa, N. Bahadur, M.S. Goyat, Influence of Fe doping on nanostructures and photoluminescence of sol-gel derived ZnO, *Mater. Chem. Phys.* 114 (2009) 194-198.
- [53] M. Shahid, L. Jingling, Z. Ali, I. Shakir, M. F. Warsi, R. Parveen, M. Nadeem, Photocatalytic degradation of methylene blue on magnetically separable MgFe<sub>2</sub>O<sub>4</sub> under visible light irradiation, *Mater. Chem. Phys.* 139 (2013) 566-571.
- [54] A. Baykal, N. Kasapoglu, Y. Koseoglu, M.S. Toprak, H. Bayrakdar, CTAB-assisted hydrothermal synthesis of NiFe<sub>2</sub>O<sub>4</sub> and its magnetic characterization, *J. Alloys Compd.* 464 (2008) 514.
- [55] C.N. Chinnasamy, A. Narayanasamy, N. Ponpandian, K. Chattopadhyay, The influence of Fe<sup>3+</sup> ions at tetrahedral sites on the magnetic properties of nanocrystalline ZnFe<sub>2</sub>O<sub>4</sub>, *Mater. Sci. Eng. A* 304-306 (2001) 983-987.
- [56] M. Atif, S.K. Hasanain, M. Nadeem, *Solid State Commun.* Magnetization of sol-gel prepared zinc ferrite nanoparticles: Effects of inversion and particle size, 138 (2006) 416-421.
- [57] S. Liu, B. Yue, K. Jiao, Y. Zhou, H. He, Template synthesis of one-dimensional nanostructured spinel zinc ferrite, *Mater. Lett.* 60 (2006) 154-158.

- [58] B.P. Rao, A. Maheshkumar, K.H. Rao, Y.L.N. Murthy, O.F. Caltun, I. Dumitru, L. Spinu, Synthesis and magnetic studies of Ni-Zn ferrite nanoparticles, *J. Optoelectronic Adv. Mater.* 8 (2006) 1703-1705.
- [59] C. Prakash, J.S. Baijal, Mossbauer studies on hyperfine field measurement in titanium doped nickel-zinc ferrites, *Solid State Commun.* 50 (1984) 557-559.
- [60] W. Yan, W. Jiang, Q. Zhang, Y. Li, H. Wang, Structure and magnetic properties of nickel-zinc ferrite microspheres synthesized by solvothermal method, *Mater. Sci. Eng. B* 171 (2010) 144-148.
- [61] A. Kumar, A. Singh, M.S. Yadav, M. Arora, R.P. Pant, Finite size effect on Ni doped nanocrystalline  $\text{Ni}_x\text{Zn}_{1-x}\text{Fe}_2\text{O}_4$  ( $0.1 \leq x \leq 0.5$ ), *Thin Solid Films* 519 (2010) 1056-1058.
- [62] Y. Koseoglu, A. Baykal, M. S. Toprak, F. Gozuak, A. C. Basaran, B. Aktas, Synthesis and characterization of  $\text{ZnFe}_2\text{O}_4$  magnetic nanoparticles via a PEG-assisted route, *J. Alloys Compd.* 462 (2008) 209-213.
- [63] A.K.M. A. Hossain, S.T. Mahmud, M. Seki, T. Kawai, H. Tabata, Structural, electrical transport, and magnetic properties of  $\text{Ni}_{1-x}\text{Zn}_x\text{Fe}_2\text{O}_4$ , *J. Magn. Magn. Mater.* 312 (2007) 210-219.
- [64] Y. Ichiyanagi, T. Uehashi, S. Yamada, Magnetic properties of Ni-Zn ferrite nanoparticles, *Phys. Stat. Solid C* 12 (2004) 3485-3488.
- [65] X. Li, Y. Hou, Q. Zhao, L. Wang, A general, one-step and template-free synthesis of sphere-like zinc ferrite nanostructures with enhanced photocatalytic activity for dye degradation, *J. Colloid Interf. Sci.* 358 (2011) 102-108.

- [66] Z. Jia, D. Ren, Y. Liang, R. Zhu, A new strategy for the preparation of porous zinc ferrite nanorods with subsequently light-driven photocatalytic activity, *Mater. Lett.* 65 (2011) 3116-3119.
- [67] Y. Zheng, C. Chen, Y. Zhan, X. Lin, Q. Zheng, K. Wei, J. Zhu, Y. Zhu, Luminescence and photocatalytic activity of ZnO nanocrystals: correlation between structure and property, *Inorg. Chem.* 46 (2007) 6675-6682.
- [68] M. Tsukada, K. Abe, Y. Yonemochi, A. Ameyama, H. Kamiya, S. Kambara, Dry gas cleaning in coal gasification systems for fuel cells using composite sorbents, *Powder Technol.* 180 (2008) 232.
- [69] P. Xiong, J. Zhu, X. Wang, Cadmium sulfide-ferrite nanocomposite as a magnetically recyclable photocatalyst with enhanced visible-light-driven photocatalytic activity and photostability, *Ind. Eng. Chem. Res.* 52 (2013) 17126-17133.
- [70] S.K. Pardeshi, A.B. Patil, Effect of morphology and crystallite size on solar photocatalytic activity of zinc oxide synthesized by solution free mechanochemical method, *J. Mol. Cat. A Chem.* 308 (2009) 32-40.
- [71] S. Ahmed, M. G. Rasul, R. Brown, M. A. Hashib, Influence of parameters on the heterogeneous photocatalytic degradation of pesticides and phenolic contaminants in waste water: a short review, *J. Environ. Manage.* 92 (2011)311-330.
- [72] J. Sun, L. Qiao, S. Sun, G. Wang, Photocatalytic degradation of Orange G on nitrogen-doped TiO<sub>2</sub> catalysts under visible light and sunlight irradiation, *J. Hazard. Mater.* 155 (2008) 312-319.

[73] M. Huang, C. Xu, Z. Wu, Y. Huang, J. Lin, J. Wu, Photocatalytic discolorization of methyl orange solution by Pt modified TiO<sub>2</sub> loaded on natural zeolite, *Dyes Pigm.* 77 (2008) 327-334.

[74] N. Venkatachalam, M. Palanichamy, V. Murugesan, Sol-gel preparation and characterization of alkaline earth metal doped nano TiO<sub>2</sub>: Efficient photocatalytic degradation of 4-chlorophenol, *J. Mol. Catal. A: Chem.* 273 (2007) 177-185.

[75] S. Anandan, A. Vinu, N. Venkatachalam, B. Arabindoo, V. Murugesan, 2006. Photocatalytic activity of ZnO impregnated H $\beta$  and mechanical mix of ZnO/H $\beta$  in the degradation of monocrotophos in aqueous solution. *J. Mol. Catal. A: Chem.* 256 (2006) 312-320.

Table 1. Lattice parameter, crystallite size (Scherer formula, Rietveld analysis) and band gap energy of  $\text{Mn}_x\text{Zn}_{1-x}\text{Fe}_2\text{O}_4$  ( $x = 0.0, 0.1, 0.2, 0.3, 0.4$  and  $0.5$ ) NCs.

Samples	Lattice parameter (Å) Rietveld analysis	Crystallite size D (nm)		Band gap (eV)	Strain (%)	S (Goodness of fit)
		Scherrer formula	Rietveld analysis			
$\text{ZnFe}_2\text{O}_4$	8.442	23.25	24	1.95	0.068	1.172
$\text{Mn}_{0.1}\text{Zn}_{0.9}\text{Fe}_2\text{O}_4$	8.444	22.03	22	2.01	0.067	1.135
$\text{Mn}_{0.2}\text{Zn}_{0.8}\text{Fe}_2\text{O}_4$	8.445	19.56	20	2.15	0.064	1.094
$\text{Mn}_{0.3}\text{Zn}_{0.7}\text{Fe}_2\text{O}_4$	8.447	17.53	17	2.27	0.061	1.103
$\text{Mn}_{0.4}\text{Zn}_{0.6}\text{Fe}_2\text{O}_4$	8.449	17.92	18	2.31	0.059	1.106
$\text{Mn}_{0.5}\text{Zn}_{0.5}\text{Fe}_2\text{O}_4$	8.451	18.36	19	2.4	0.057	1.104

Table 2. Variation of coercivity ( $H_c$ ), remanant magnetization ( $M_r$ ) and saturation magnetization ( $M_s$ ) of  $Mn_xZn_{1-x}Fe_2O_4$  ( $x = 0.0, 0.1, 0.2, 0.3, 0.4$  and  $0.5$ ) NCs.

Samples	$H_c$ (Oe)	$M_r$ (emu/g)	$M_s$ (emu/g)
$ZnFe_2O_4$	$6.073 \pm 09$	$0.029 \pm 01$	$6.928 \pm 03$
$Mn_{0.1}Zn_{0.9}Fe_2O_4$	$20.75 \pm 17$	$0.196 \pm 02$	$24.33 \pm 08$
$Mn_{0.2}Zn_{0.8}Fe_2O_4$	$26.56 \pm 06$	$1.235 \pm 02$	$37.77 \pm 15$
$Mn_{0.3}Zn_{0.7}Fe_2O_4$	$36.75 \pm 13$	$5.553 \pm 12$	$45.17 \pm 13$
$Mn_{0.4}Zn_{0.6}Fe_2O_4$	$55.88 \pm 11$	$9.575 \pm 15$	$55.24 \pm 02$
$Mn_{0.5}Zn_{0.5}Fe_2O_4$	$67.35 \pm 14$	$13.88 \pm 08$	$67.38 \pm 11$

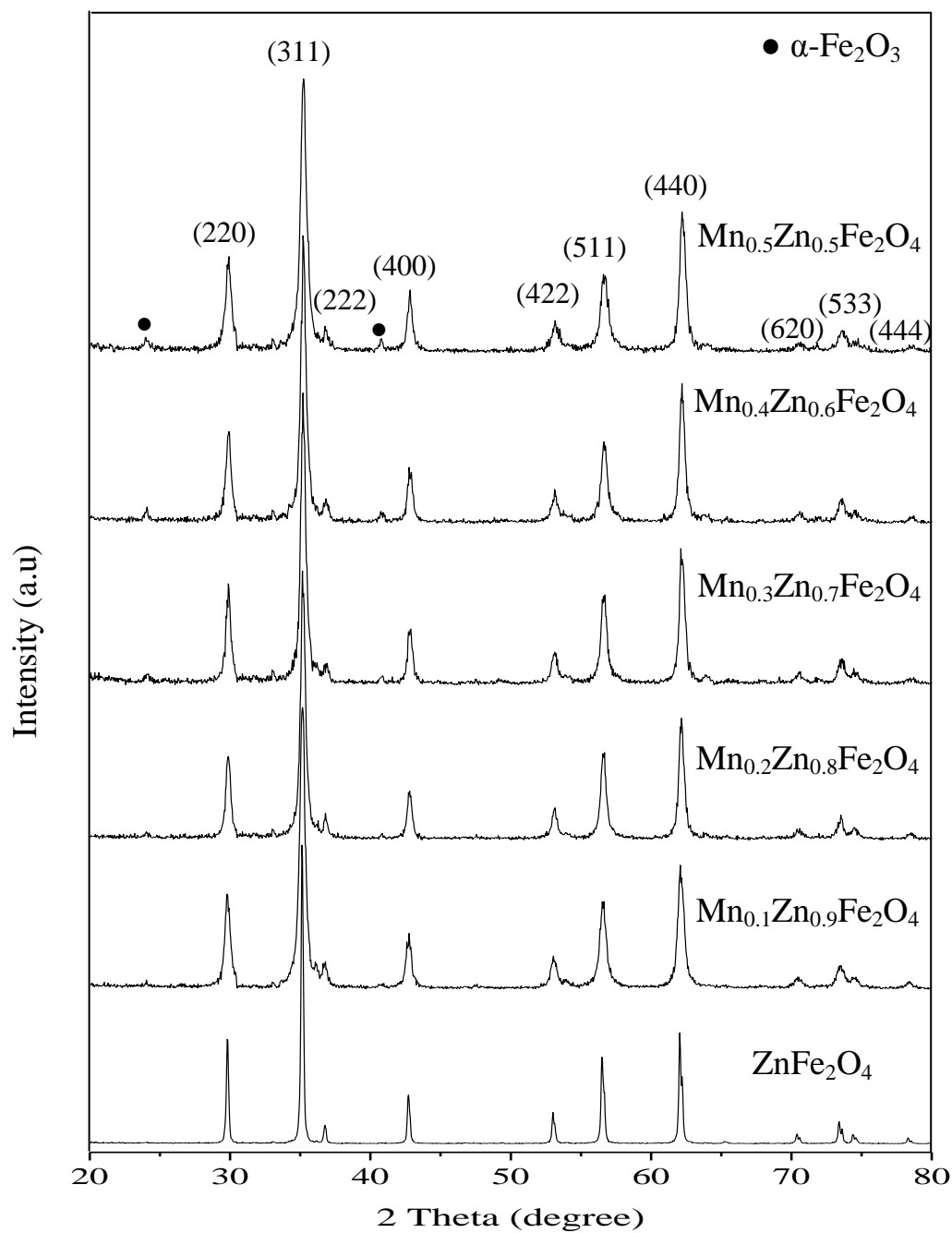


Figure 1. XRD patterns of  $\text{Mn}_x\text{Zn}_{1-x}\text{Fe}_2\text{O}_4$  ( $x = 0.0, 0.1, 0.2, 0.3, 0.4$  and  $0.5$ ) NCs.

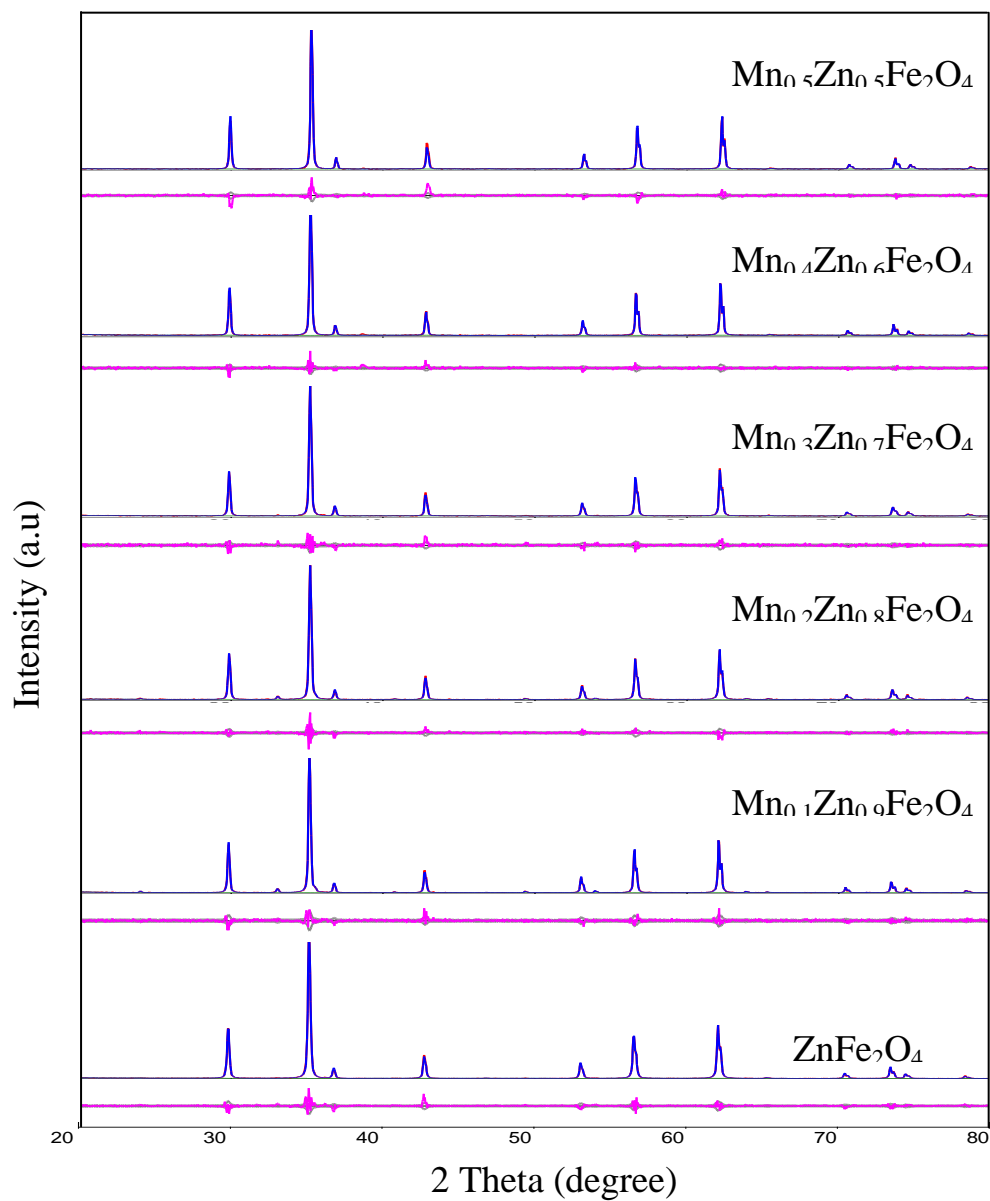


Figure 2. XRD pattern refinements using the Rietveld method of  $\text{Mn}_x\text{Zn}_{1-x}\text{Fe}_2\text{O}_4$  ( $x = 0.0, 0.1, 0.2, 0.3, 0.4$  and  $0.5$ ) NCs (Experimental data, upper solid line: calculated pattern, lower solid line: intensity difference).

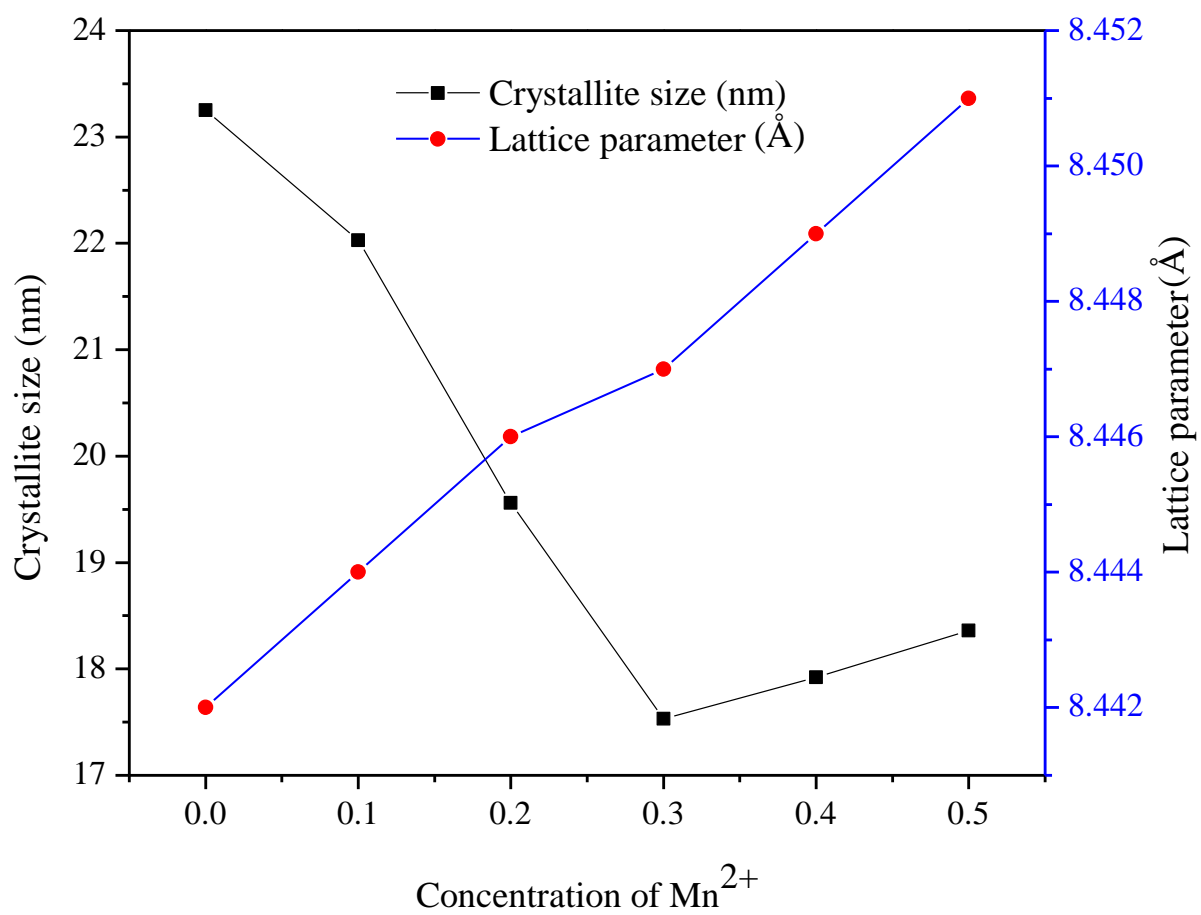


Figure 3. Evolution of the lattice parameter and crystallite size of  $\text{Mn}_x\text{Zn}_{1-x}\text{Fe}_2\text{O}_4$  ( $x = 0.0, 0.1, 0.2, 0.3, 0.4$  and  $0.5$ ) NCs.

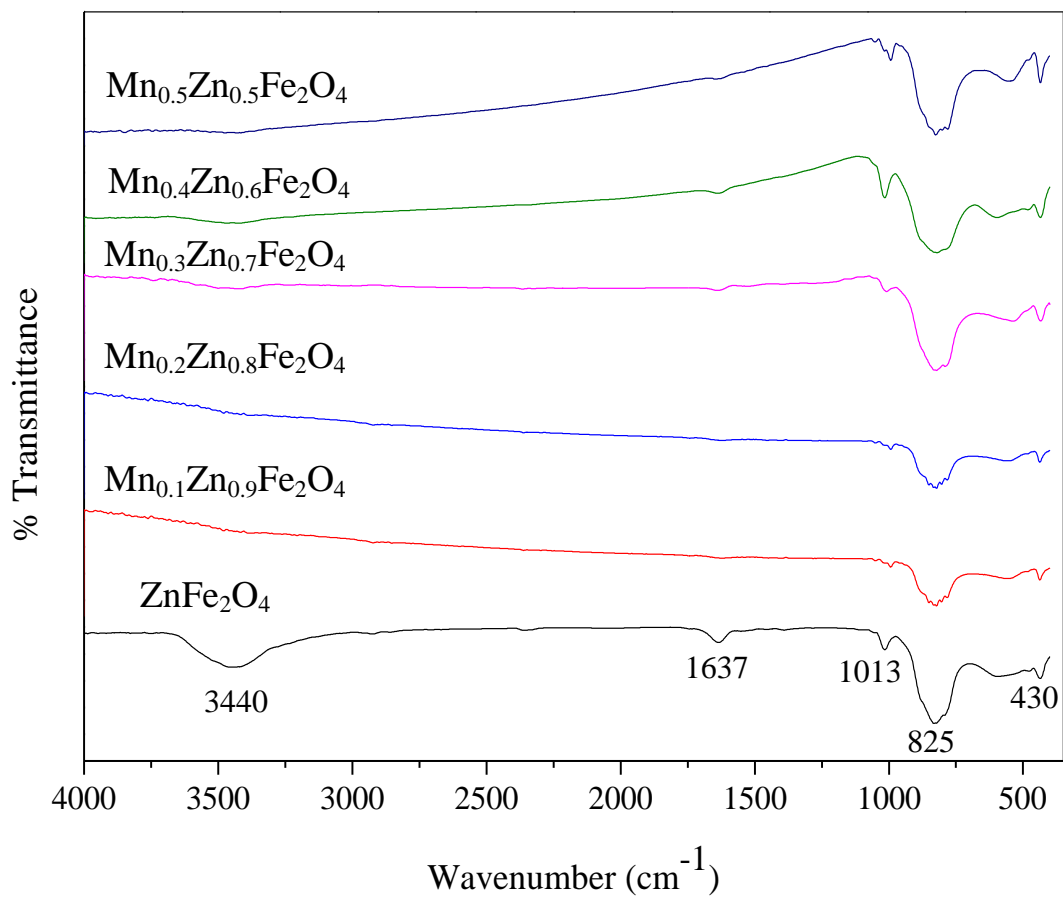


Figure 4. FT-IR analysis of Mn<sub>x</sub>Zn<sub>1-x</sub>Fe<sub>2</sub>O<sub>4</sub> ( $x = 0.0, 0.1, 0.2, 0.3, 0.4$  and  $0.5$ ) NCs.

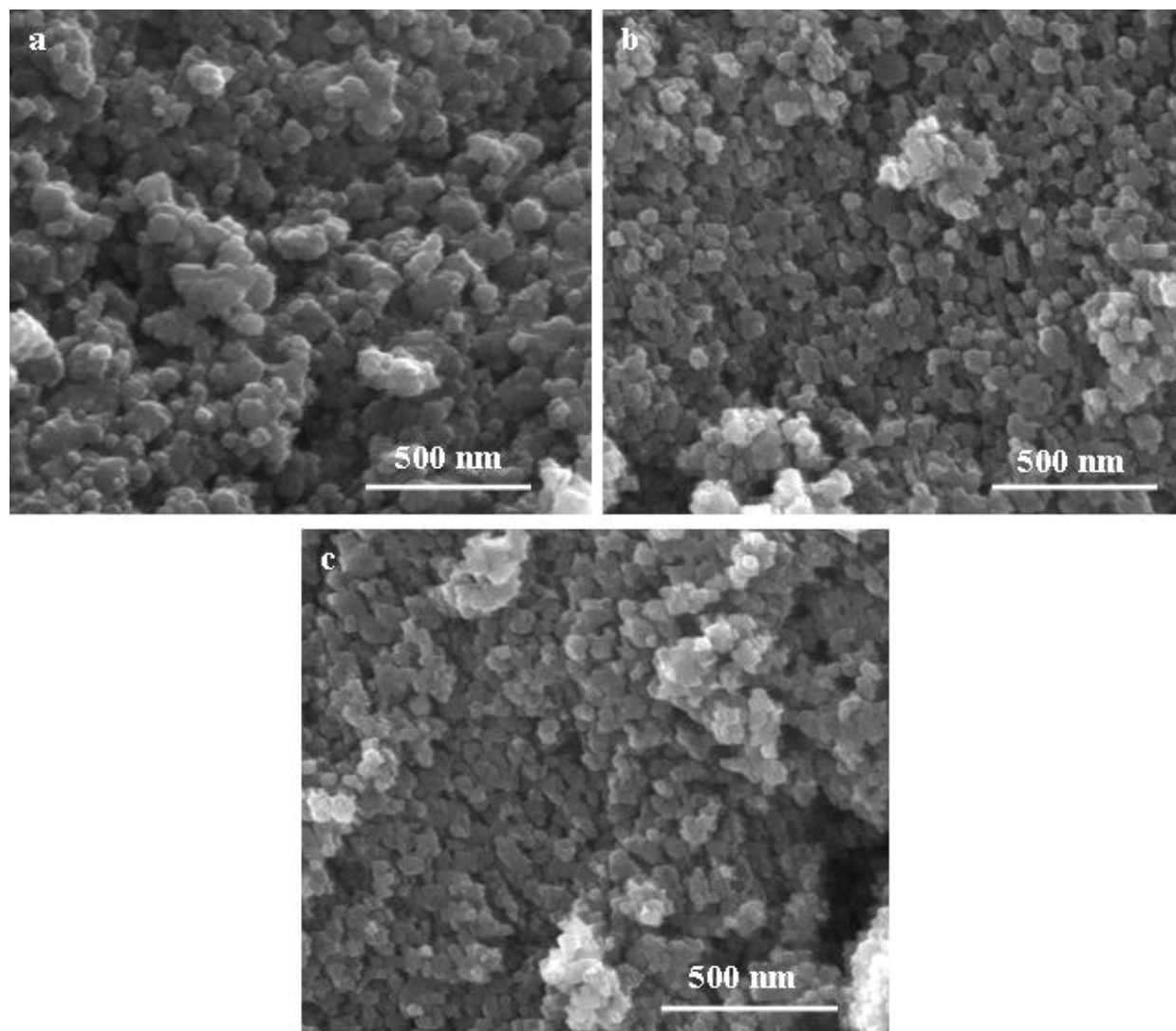


Figure 5. HR-SEM images of (a) ZnFe<sub>2</sub>O<sub>4</sub>, (b) Mn<sub>0.3</sub>Zn<sub>0.7</sub>Fe<sub>2</sub>O<sub>4</sub> and (c) Mn<sub>0.5</sub>Zn<sub>0.5</sub>Fe<sub>2</sub>O<sub>4</sub> NCs.

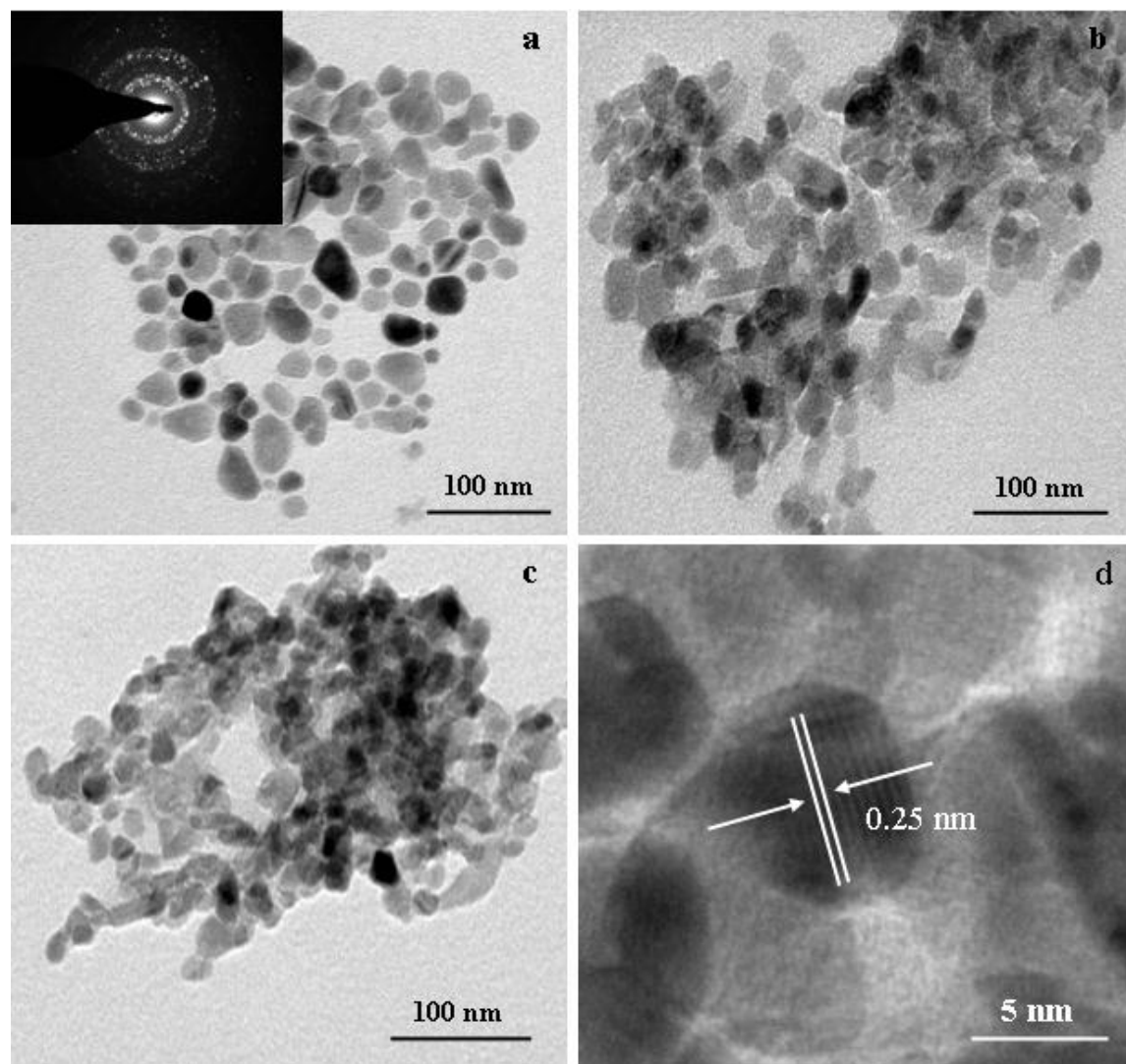


Figure 6. HR-TEM image of (a,d)  $\text{ZnFe}_2\text{O}_4$ , (b)  $\text{Mn}_{0.3}\text{Zn}_{0.7}\text{Fe}_2\text{O}_4$  and (c)  $\text{Mn}_{0.5}\text{Zn}_{0.5}\text{Fe}_2\text{O}_4$  NCs, inset Fig. 6a SAED patterns  $\text{Mn}_{0.5}\text{Zn}_{0.5}\text{Fe}_2\text{O}_4$  NCs.

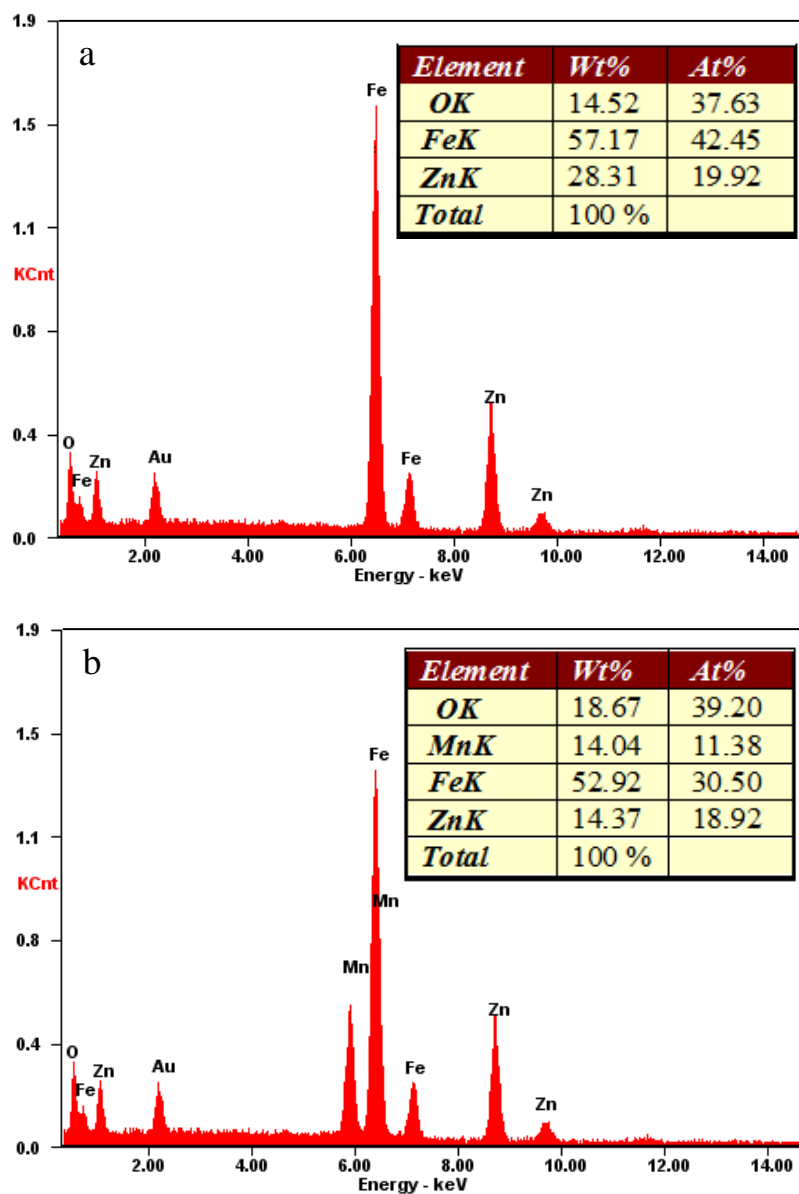


Figure 7. EDX spectra of (a)  $\text{ZnFe}_2\text{O}_4$  and (b)  $\text{Mn}_{0.5}\text{Zn}_{0.5}\text{Fe}_2\text{O}_4$  NCs.

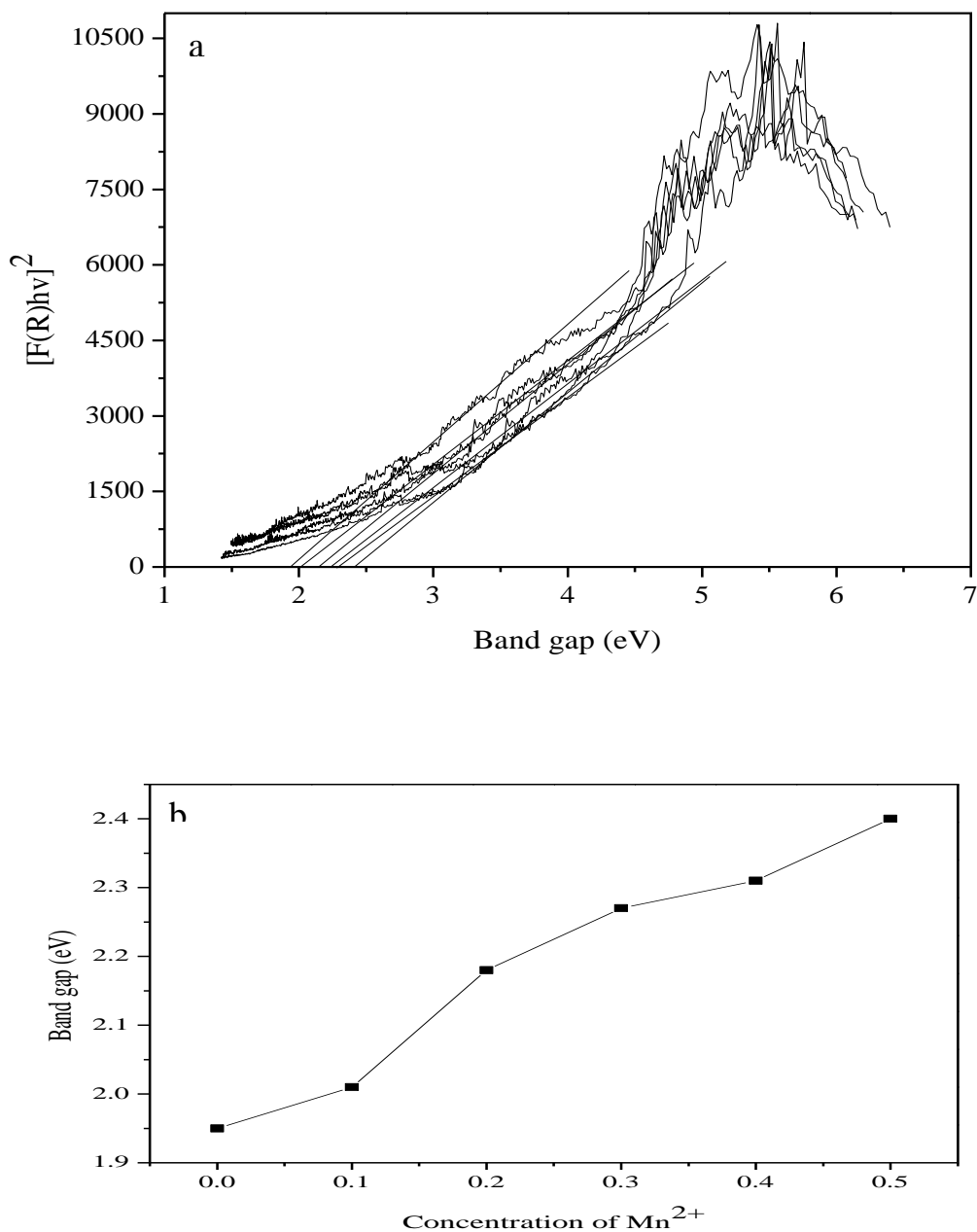


Figure 8. UV-Vis reflectance spectra of  $\text{Mn}_x\text{Zn}_{1-x}\text{Fe}_2\text{O}_4$  ( $x = 0.0, 0.1, 0.2, 0.3, 0.4$  and  $0.5$ ) NCs (Fig. 8a), and the variation of the band gap of  $\text{Mn}_x\text{Zn}_{1-x}\text{Fe}_2\text{O}_4$  ( $x = 0.0, 0.1, 0.2, 0.3, 0.4$  and  $0.5$ ) NCs (Fig. 8b).

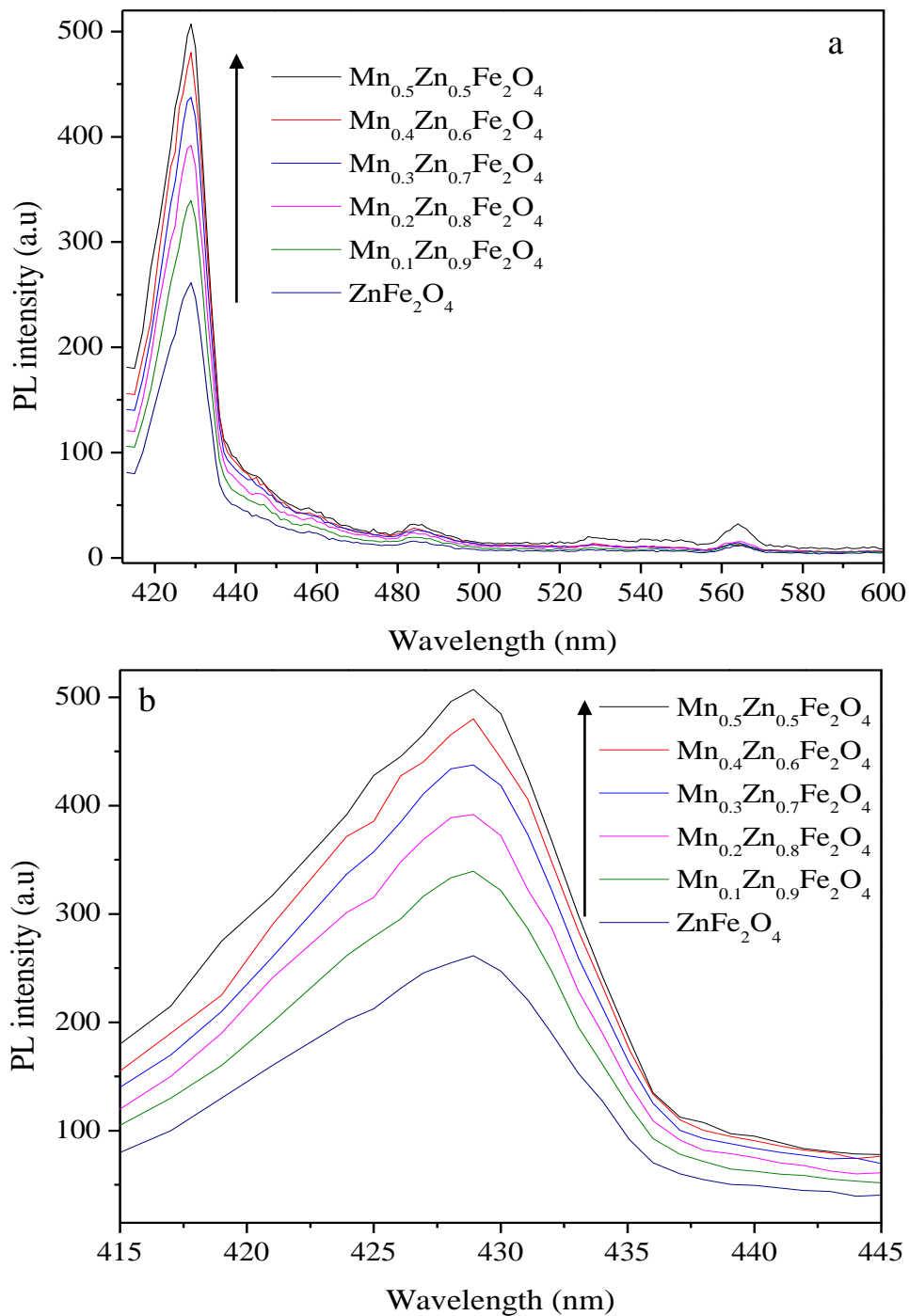


Figure 9. PL spectra of  $\text{Mn}_x\text{Zn}_{1-x}\text{Fe}_2\text{O}_4$  ( $x = 0, 0.1, 0.2, 0.3, 0.4$  and  $0.5$ ) NCs.

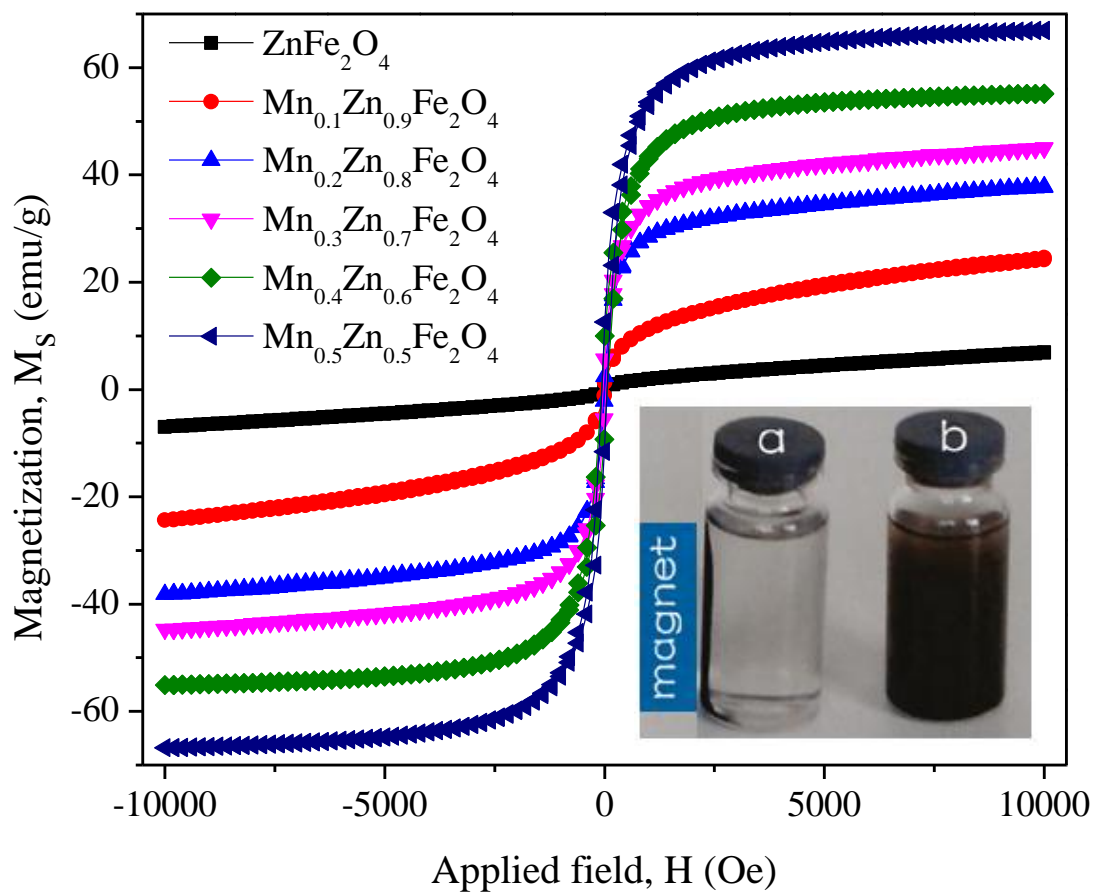


Figure 10. Magnetic hysteresis (M-H) loops of  $\text{Mn}_x\text{Zn}_{1-x}\text{Fe}_2\text{O}_4$  ( $x = 0.0, 0.1, 0.2, 0.3, 0.4$  and  $0.5$ ) NCs.

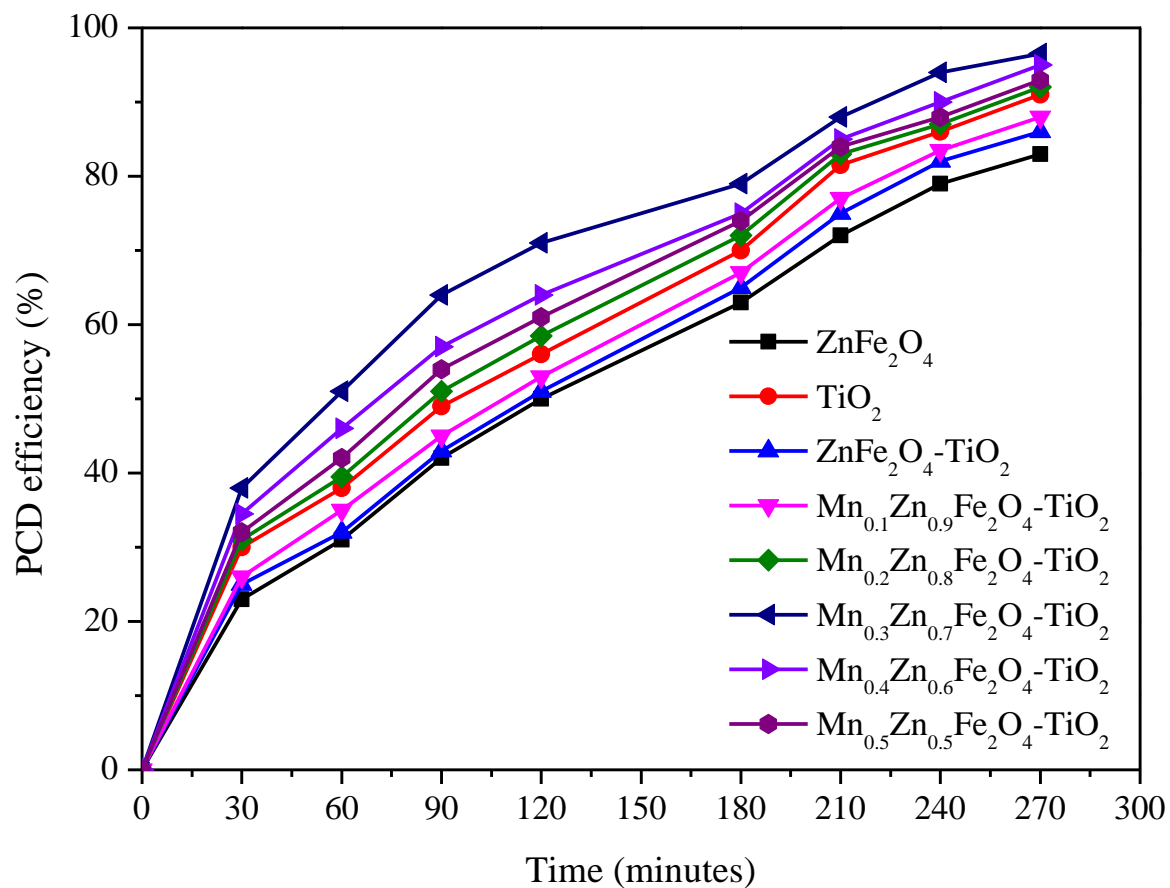


Figure 11. Effect of Mn doping on the PCD efficiency of TiO<sub>2</sub>-supported ZnFe<sub>2</sub>O<sub>4</sub> photocatalyst (Experimental conditions: 4-CP = 200 mg/L, Photocatalyst = 30 mg/100 mL,  $\lambda = 365$  nm, pH of suspension = 8).

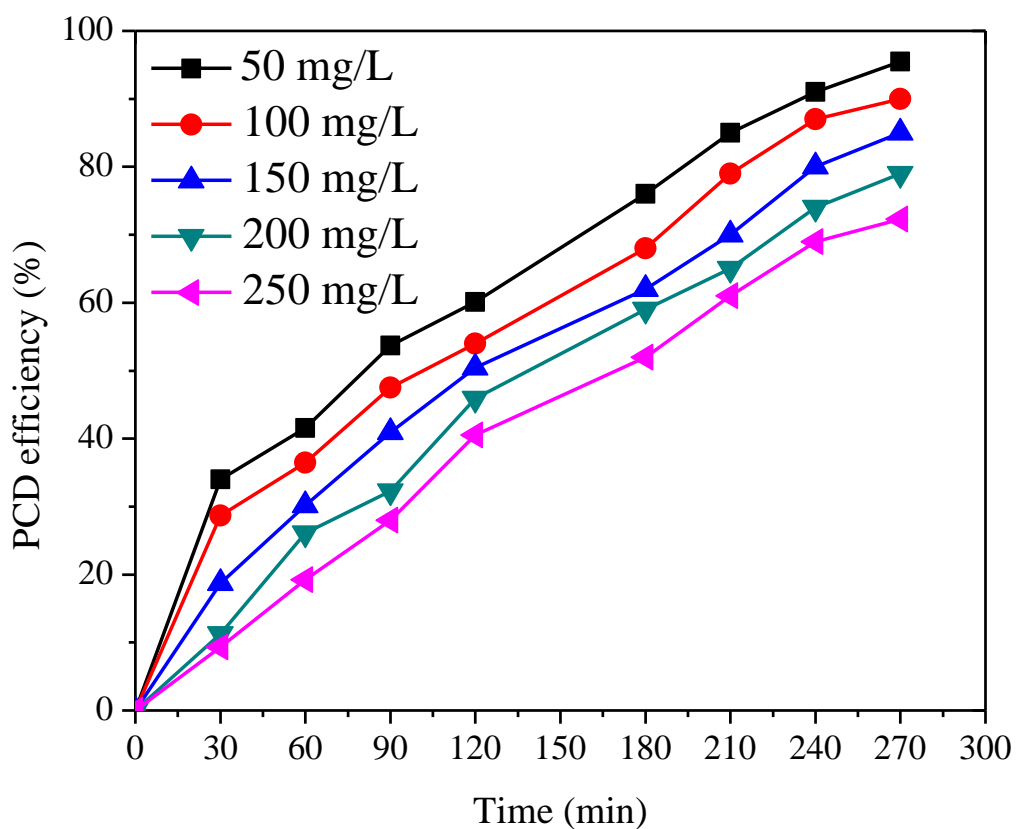


Figure 12. Effect of the amount of photocatalyst on PCD efficiency (Experimental conditions: Photocatalyst =  $\text{ZnFe}_2\text{O}_4\text{-TiO}_2$  NCs /100 mL, 4-CP = 200 mg/L, pH of suspension = 6-6.5 (natural pH),  $k = 365$  nm).

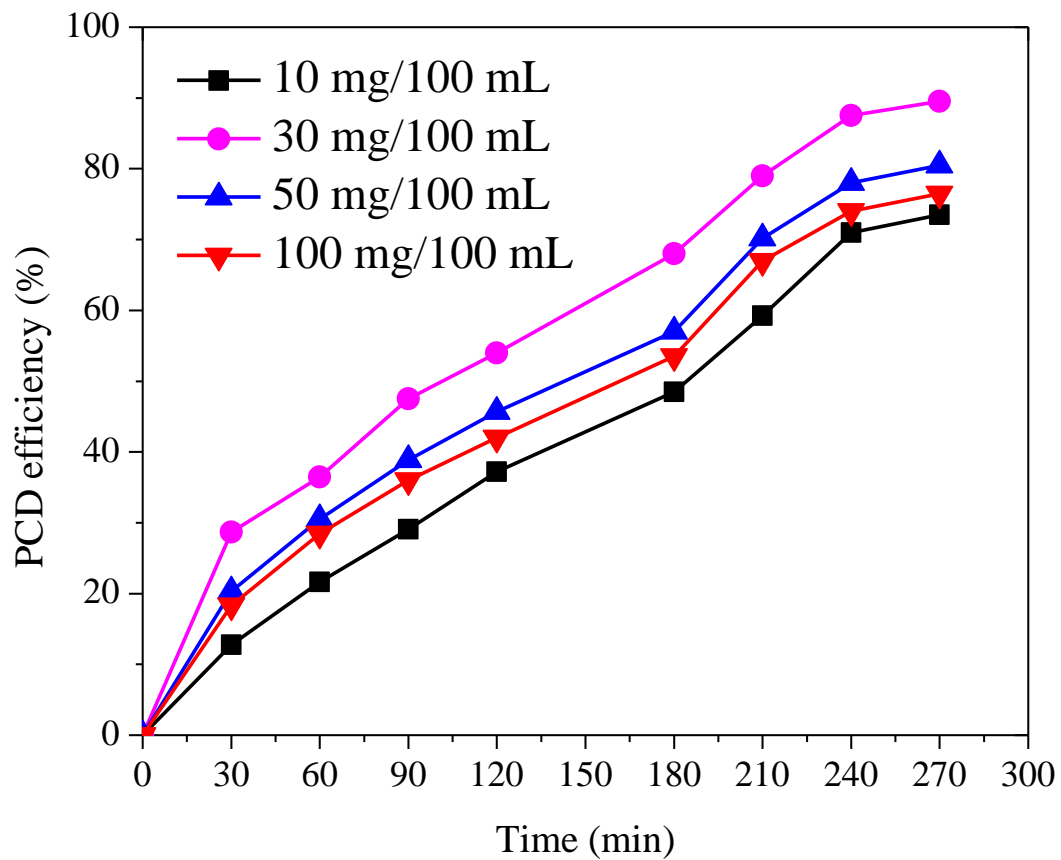
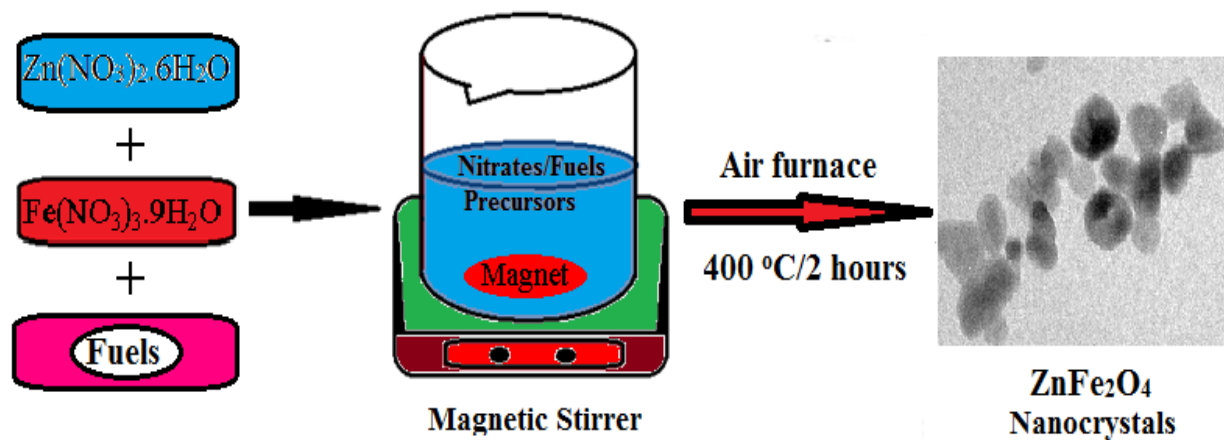
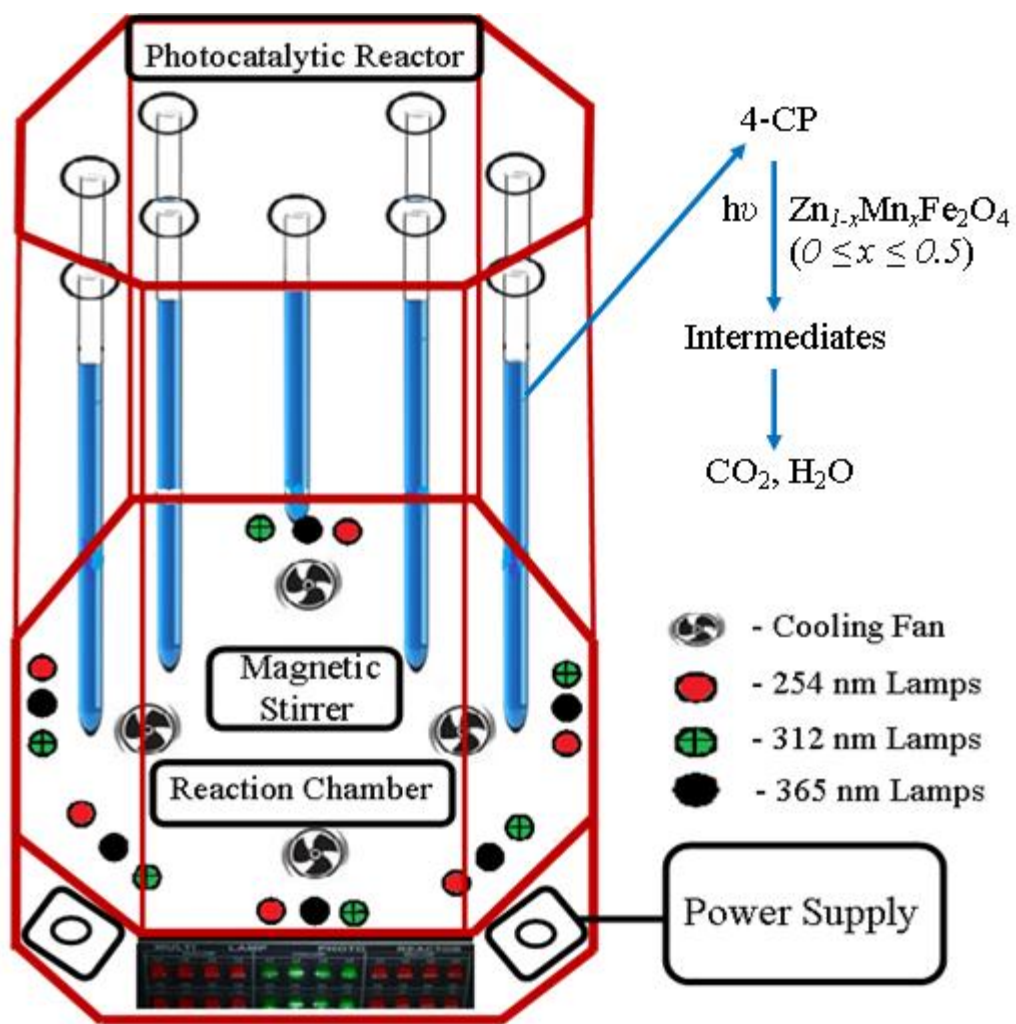


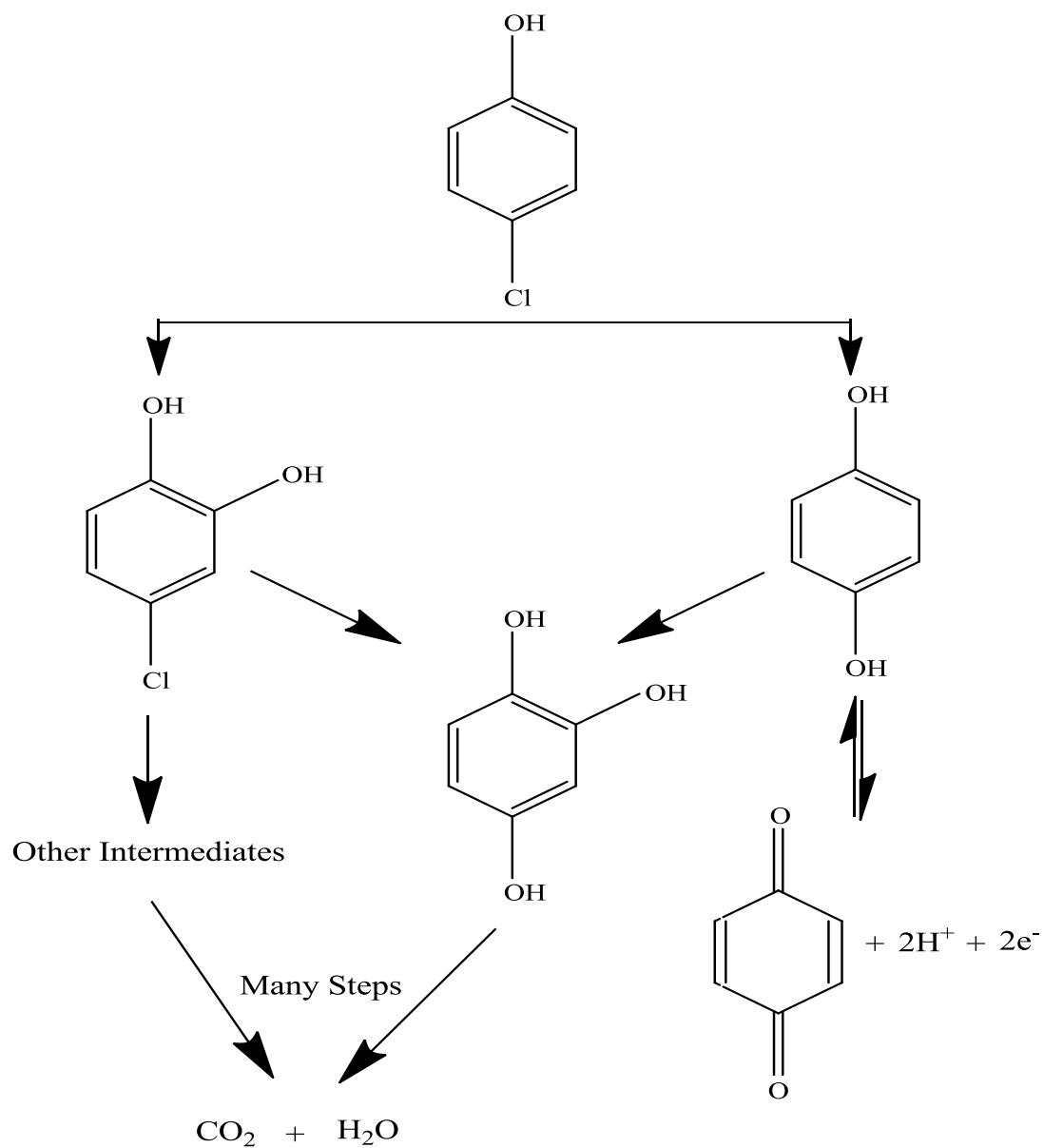
Figure 13. Effect of concentration of 4-CP on PCD efficiency (Experimental conditions:  $\text{ZnFe}_2\text{O}_4\text{-TiO}_2$  NCs = 30 mg/100 mL, initial pH of suspension = 6-6.5 (natural pH),  $k = 365$  nm).



Scheme 1. Schematic diagram of preparation procedures of  $\text{ZnFe}_2\text{O}_4$  nanostructures by a simple urea-assisted combustion method.



Scheme 2. Schematic diagram of photocatalytic reactor.



Scheme 3. Schematic diagram of proposed photo-catalytic degradation path way of 4-CP.